TAMPEREEN TEKNILLINEN YLIOPISTO
TAMPERE UNIVERSITY OF TECHNOLOGY

Mohammadhossein Behfar

Design, Development and *in vivo* Evaluation of a Wireless Platform for Intracranial Pressure Monitoring Using Inductive Passive Implants

Julkaisu 1521 • Publication 1521

Tampere 2018

Tampereen teknillinen yliopisto. Julkaisu 1521
Tampere University of Technology. Publication 1521

Mohammadhossein Behfar

Design, Development and *in vivo* Evaluation of a Wireless Platform for Intracranial Pressure Monitoring Using Inductive Passive Implants

Thesis for the degree of Doctor of Science in Technology to be presented with due permission for public examination and criticism in Sähkötalo Building, Auditorium S203, at Tampere University of Technology, on the 9th of February 2018, at 12 noon.

Tampereen teknillinen yliopisto - Tampere University of Technology
Tampere 2018

Doctoral candidate:	Mohammadhossein Behfar Wireless Identification and Sensing Systems Research Group Faculty of Biomedical Engineering and Sciences Tampere University of Technology Finland
Supervisor:	Leena Ukkonen, Prof., Dr. Tech. Wireless Identification and Sensing Systems Research Group Faculty of Biomedical Engineering and Sciences Tampere University of Technology Finland
Instructor:	Lauri Sydänheimo, Prof., Dr. Tech. Wireless Identification and Sensing Systems Research Group Faculty of Biomedical Engineering and Sciences Tampere University of Technology Finland
Pre-examiners:	Karu Esselle, Prof. Faculty of Science and Engineering Macquarie University Australia Ville Viikari, Assoc. Prof. Department of Electronics and Nanotechnology Aalto University Finland
Opponent:	Smail Tedjini, Prof. Grenoble Institute of Technology | Grenoble INP France

ISBN 978-952-15-4074-5 (printed)
ISBN 978-952-15-4092-9 (PDF)
ISSN 1459-2045

Abstract

Implantable LC-based passive sensors can enable wireless measurement of physiological parameters in inaccessible locations of the human body through an RF inductive link. A typical LC sensor consists of an inductive coil connected to a capacitive pressure sensing element to form an LC resonator, whose resonance frequency changes in response to variation of the quantity being measured. In biomedical applications, they are intended to provide continuous measurement of the desired parameter in patients with chronic diseases without the need for an implanted battery. Considering their cost-efficient manufacturing and fully passive operation, they are considered promising alternatives to the existing catheter-based transducers and can be potentially used in a variety of applications, including intraocular pressure (IOP) monitoring, intracranial pressure (ICP) monitoring and cardiovascular pressure sensing.

Over the past few decades, there has been increasing number of research in the development of fully passive pressure sensors for biomedical applications. Although the previous studies advanced the possibility of wireless pressure readout across the tissue, further development is required to translate the concept to clinically approved devices. In this research work, a complete system for biotelemetric wireless ICP monitoring was designed, developed and evaluated through *in vitro* and *in vivo* studies. The proposed system includes an ICP implant, which is wirelessly interrogated by a hand-held external reader. The external reader communicates with the implant through separated wireless channels for concurrent excitation of the implant and collection of the received signal from the sensor. The simultaneous transmit and receive operation is realized through a novel dual-port planar antenna. The reader device is connected to a host PC through a Bluetooth link. The proposed system provides real-time monitoring of the ICP through a dedicated interactive PC software.

The *in vivo* performance of the implant was evaluated in a canine model. The findings of the *in vivo* study are consistent with the theoretical analysis of the proposed telemetry scheme as well as the data obtained from the *in vitro* experiments. The capability of the wireless pressure readout and detection of *in vivo* ICP variation has been proved through the animal study and the *in vivo* data was verified using a commercial ICP monitor. The promising outcome of the in-body assessment of the system indicates that the proposed platform can be further developed and potentially used in real-life clinical trials for early detection of increasing ICP in patients with traumatic brain injuries and chronic intracranial hypertension. In addition, the same platform with further modification and customization can be used for other biomedical applications.

Preface

This research work was conducted at the Department of Electronics and Communications between years 2014-2016 and then at the Faculty of Biomedical Engineering and Sciences at Tampere University of Technology in Finland in 2017. This doctoral study was supported in part by Academy of Finland, in part by Jane and Aatos Erkko Foundation, in part by the Finnish Agency for Technology and Innovation (TEKES), in part by Tekniikan edistämissäätiö (TES) and in part by US FDA Grant.

Special thanks to my supervisor, Professor Leena Ukkonen, and my instructor, Professor Lauri Sydänheimo, for their support and excellent provision of the research facilities during my research work. I appreciate all their contributions to my doctoral studies. My sincere gratitude goes to Professor Shuvo Roy for his welcoming attitude during my visit at the Biodesign Lab at University of California, San Francisco (UCSF). His valuable support and guidance are unforgettable. I also appreciate all my co-workers and co-authors for every effort they made for the good of my research.

My deepest appreciation goes to my parents for their unconditional love, best wishes and endless support. Lastly, my heartfelt thanks go to my beloved wife, who opened a new chapter of love and kindness in my life.

Tampere, November 2017

Mohammadhossein Behfar

Table of Contents

List of Symbols and Abbreviations

AC	Alternating Current
ADC	Analog to Digital Converter
BT	Bluetooth
CSF	Cerebrospinal Fluid
DC	Direct Current
DDS	Direct Digital Synthesizer
DMA	Direct Memory Access
EEG	Electroencephalography
EM	Electromagnetic
FDA	Food and Drug Administration
HF	Heart Failure
IACUC	Institutional Animal Care and Use Committee
ICP	Intracranial Pressure
IDE	Integrated Development Environment
IH	Intracranial Hypertension
IMD	Implantable Medical Device
IOP	Intraocular Pressure
LC	Inductive-Capacitive
MCU	Microcontroller Unit
MEMS	Microelectromechanical Systems
MRI	Magnetic Resonance Imaging

PC	Personal Computer
PDMS	Polydimethylsiloxane
RF	Radio Frequency
TBI	Traumatic Brain Injury
T/R	Transmit/Receive
UART	Universal Asynchronous Receiver/Transmitter
VNA	Vector Network Analyzer
WPT	Wireless Power Transmission
3D	Three-Dimensional Space

List of Publications

· The thesis is based on the extended summary of the following publications. The papers are listed in order in which they are cited in the thesis manuscript.

I. **M. H. Behfar**, T. Björninen, E. Moradi, L. Sydänheimo and L. Ukkonen, "Biotelemetric Wireless Intracranial Pressure Monitoring: An In Vitro Study," International Journal of Antennas and Propagation, vol. 2015, Article ID 918698, 10 pages, Nov. 2015.

II. **M. H. Behfar**, L. Sydänheimo, S. Roy, and L. Ukkonen, "Dual-Port Planar Antenna for Implantable Inductively Coupled Sensors," IEEE Transaction on Antennas and Propagation, vol. 65, no. 11, pp. 5732–5739, Nov. 2017.

III. **M. H. Behfar**, E. Abada, L. Sydänheimo, K. Goldman, A. J. Fleischman, N. Gupta, L. Ukkonen, and Shuvo Roy, "Inductive passive sensor for intraparenchymal and intraventricular monitoring of intracranial pressure," in 2016 IEEE 38th Annual International Conference of the Engineering in Medicine and Biology Society (EMBC), pp. 1950–1954, 2016.

IV. M. W. A. Khan, **M. H. Behfar**, T. Björninen, L. Sydänheimo, and L. Ukkonen, "Effect of magnetic core and higher operational frequency on sensitivity in frequency shift detection in wireless passive minimally invasive Intracranial Pressure Monitoring," in 2015 International Conference on Electromagnetics in Advanced Applications (ICEAA), pp. 383–386, 2015.

V. **M. H. Behfar**, E. Moradi, T. Björninen, L. Sydänheimo, and L. Ukkonen, "Design and Technical Evaluation of an Implantable Passive Sensor for Minimally Invasive Wireless Intracranial Pressure Monitoring," in World Congress on Medical Physics and Biomedical Engineering, Toronto, Canada, D. A. Jaffrey, Ed. Springer International Publishing, pp. 1301–1304, 2015.

· The following papers were published during this doctoral research, but not included in the dissertation:

I. **M. H. Behfar**, L. Sydänheimo, L. Ukkonen, A. J. Fleischman, H. Jiang, and S. Roy, "Optimization of orthogonal-coil RF probe for miniature passive implantable pressure sensors," in 2016 IEEE International Symposium on Antennas and Propagation (APSURSI), pp. 1047–1048, 2016.

II. **M. H. Behfar,** E. Moradi, T. Björninen, L. Sydänheimo and L. Ukkonen, "Evaluation of an implantable passive sensor for wireless intracranial pressure monitoring," in 2015 IEEE International Symposium on Antennas and Propagation USNC/URSI National Radio Science Meeting, pp. 1201–1202, 2015.

III. M. W. A. Khan, M. Rizwan, **M. H. Behfar**, L. Sydänheimo, T. Björninen, and L. Ukkonen, "Effect of implant coating on wireless powering for intracranial pressure monitoring system," in 2017 IEEE International Symposium on Antennas and Propagation USNC/URSI National Radio Science Meeting, pp. 389–390, 2017.

1 Introduction

There are medical scenarios in which continuous in-body measurement of physiological parameters is essential. In those cases, depending on the medical need, a catheter-based transducer may be introduced into the body to measure the target parameter. In general, catheterization is an established method for insertion of miniature biomedical transducers inside the human body. However, the catheter-based measurements are intermitted and may require connection to an external device. Moreover, they are associated with the risk of infection, trauma and hemorrhage. To mitigate the complications of the catheter-based in-body measurements, implantable sensing devices were developed to provide long-term continuous monitoring of physiological parameters in challenging locations of the human body.

1.1 Wireless biomedical implants for sensing applications

Traditionally, wireless implantable medical devices (IMDs) have been powered using implanted batteries, and therefore, various types have been designed and developed for implantable devices [1]–[9]. However, the key challenge with the battery-powered implants is the increased size of the device due to the battery. Moreover, the lifetime of the implant depends on the lifetime of the battery. In addition to aforementioned complications, the implanted batteries may also raise issues concerning patient safety and biocompatibility [10]. To overcome the limitations of the battery-powered implants, wirelessly powered implants were developed to power an implant across tissue and eliminate the need for an implanted battery. There are various strategies for wireless power transmission (WPT) to an implanted device including ultrasonic [11]–[14], near-field [15]–[21], mid-field [22] and far-field [23],[24] coupled WPT. Among the aforementioned methods of WPT, the near-field inductive resonant coupling is the most common and established method used in FDA approved devices [25], [26].

Over the last few decades, there has been a growing interest in the utilization of LC-based passive implantable sensors to measure physiological parameters in inaccessible locations of the human body [27]–[44]. They benefit from fully passive operation and are built to operate *in vivo* without the need for implanted battery and active components [45]. A typical LC-based passive sensor consists of an inductive coil and a variable capacitive sensing element. The inductance of the coil and capacitance of the sensing element creates an LC tank, whose resonance frequency changes in response to the variations of the quantity being measured (e.g. pressure, temperature, flow, strain etc.).

Considering their fully passive operation, as well as minimally invasive implantation of this kind of the sensors, they are considered a promising alternative to the existing catheter-based

transducers and battery-powered sensors. This type of sensors can be used in a variety of applications including intraocular pressure (IOP) monitoring for Glaucoma, intracranial pressure monitoring (ICP) in patients suffering from traumatic brain injury (TBI), cardio vascular pressure sensing and evaluation of progressive spinal perfusion [31], [39]. Previous studies reported several LC-based sensors for specific applications. In [38], Chitnis et al. reported a passive IOP sensor for monitoring the pressure inside the eye. The proposed sensor was evaluated *in vivo* through animal tests in rabbits. The animal study showed that the proposed sensor remains functional *in vivo* for a month. In another study [37], Chen et al. reported a mm-size passive ICP implant for continuous subdural ICP monitoring. The proposed sensor was implanted in the subdural region, and pressure variation was detected through an external reader antenna. The sensor was evaluated through an *in vivo* experiment using a rodent model. In [39], a fully passive LC sensor was developed by Ferrara et al. to conduct a biomechanical study for the evaluation of progressive spinal fusion.

In addition to the LC-based sensors developed in the aforementioned studies, CardioMEMS (acquired by St. Jude Medical) introduced the EndoSensor/CardioMEMS HF System, the first FDA-approved heart failure (HF) system for detection of HF within the pulmonary artery [46].

1.2 Fully passive implant for ICP measurement

Increased ICP is a neurological disorder, which is commonly caused by cerebral edema, cerebrospinal fluid (CSF) disorders, head injury and localized intracranial mass lesion [47]. Management of raised ICP is an urgent issue in patients with traumatic brain injuries (TBI) [48]. Unmanaged intracranial hypertension might increase the risk of severe brain damage, disability or death. In clinical practice, there are direct invasive and indirect noninvasive methods for the management of ICP. Intraventricular catheters are commonly used in clinical ICP measurement. However, catheter insertion introduces the risk of hemorrhage and infection [49], [50]. On the other hand, indirect noninvasive methods, such as magnetic resonance imaging (MRI), analysis of electroencephalograph (EEG) power spectrum, audiological and ophthalmological techniques, are less accurate compared to the invasive method [51], [52]. Recently, a noninvasive ICP monitoring device was introduced by Headsens Ltd. The ICP device uses acoustic waves to measure ICP. A low frequency acoustic signal is transmitted in one ear and received in another ear. The received signal is processed and analyzed to calculate the intracranial pressure. According to the company, analysis of the data obtained from the initial clinical trials is still in process [53].

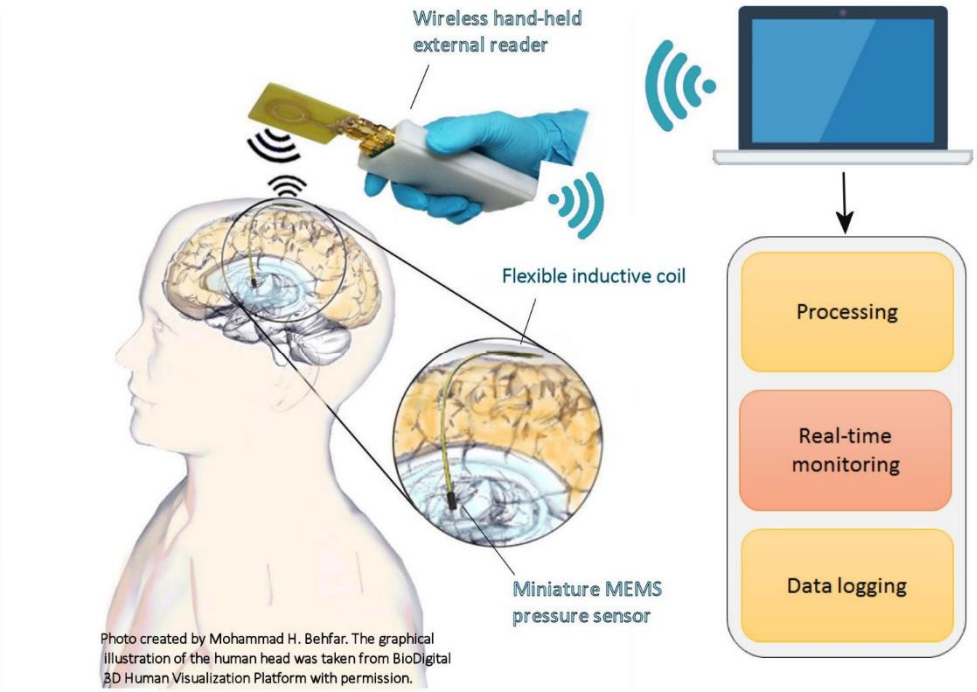

Fig. 1. Graphical illustration of the proposed ICP measurement system.

In order to mitigate the complications of the existing invasive ICP measurement methods, battery-powered implantable sensors were proposed. Kawoos et al. [54] proposed a battery-supplied implantable wireless sensor. The sensor detects ICP variations with a MEMS pressure sensor, and the measurement data is transmitted to an external unit via 2.4 GHz RF link. In another work [55], Meng et al. reported a battery-assisted implant, which detects the ICP variation through the change in oscillation frequency of an RC oscillator, which modulates a 2.4 GHz RF oscillator coupled to a planar inverted-F antenna. However, the proposed ICP sensors require an implanted power supply and, thereby, suffer from the complications mentioned in Section 1.1.

In this research, a comprehensive study on the design, development, *in vitro* and *in vivo* evaluation of a complete wireless system for continuous ICP monitoring is presented. The proposed system includes a fully passive ICP implant, an external reader device and a standalone PC application for continuous ICP monitoring to manage the physiological complications in patients with intracranial hypertension (IH). A graphical illustration of the proposed ICP system is shown in Fig.1.

1.3 Scope of the thesis

This thesis is structured into 6 chapters, as illustrated in Fig.2. Following the introduction, in Chapter 2, a comprehensive analysis of the inductive telemetry systems and principle of measurement with LC-based passive sensors is presented. In Chapter 3, the design and development of the external reader device is discussed. In addition, the design concepts for the development of a hand-held reader device is presented. In Chapters 4 and 5, *in vitro* and *in vivo* evaluation of the ICP implant are presented, respectively. The thesis concludes with the outcomes and achievements of this study in Chapter 6. Moreover, this chapter discusses future directions for the development of a clinically approved ICP implant.

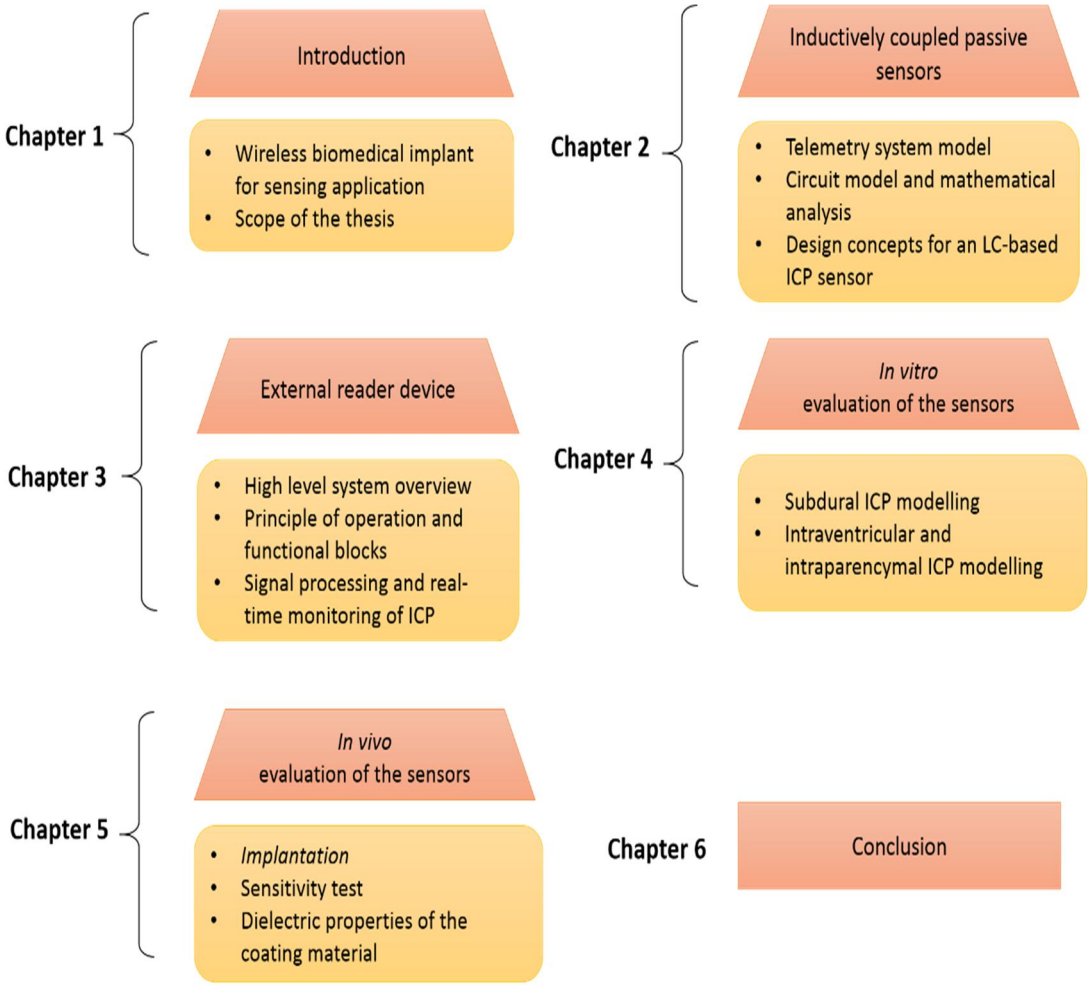

Fig. 2. Structure of the thesis.

1.4 Authors' contribution

Publication I: "Biotelemetric Wireless Intracranial Pressure Monitoring: An In Vitro Study" was published with the contribution of the author and co-authors. In the paper, the author presented the theoretical analysis of the proposed telemetry system, conducted the experiments and wrote the manuscript. Dr. Toni Björninen contributed in writing a section of the manuscript and provided the simulation results. Dr. Elham Moradi helped with some of the experiments. Professor Sydänheimo and Professor Ukkonen commented on the manuscript and improved its quality.

Publication II: "Dual-port Planar Antenna for Implantable Inductively Coupled Sensors" was submitted with the contribution of the authors and co-authors. In this paper, the author presented a theoretical analysis of the antenna performance, conducted the experiments and wrote the manuscript. The co-authors commented on the paper and improved its quality.

Publication III: "Inductive Passive Sensor for Intraparenchymal and Intraventricular Monitoring of Intracranial Pressure" was published with the contribution of the author and co-authors. In this paper, the author wrote the manuscripts, conducted the experiments and analyzed the results. Emily Abada helped with coating the ICP sensor with PDMS. She also helped with writing a sub-section of the paper. Dr. Nalin Gupta helped with the introduction of the paper. The other co-authors commented on the manuscript and helped improve the quality of the paper.

Publication IV: "Effect of Magnetic Core and Higher Operational Frequency on Sensitivity in Frequency Shift Detection in Wireless Passive Minimally Invasive Intracranial Pressure Monitoring" was published with the contribution of the author and co-authors. The author wrote the manuscript and studied the impact of the magnetic core on the sensitivity of the frequency shift in an LC tank circuit. The first co-author (M. H. Behfar) conducted the experiments, analyzed the data and wrote a section of the paper. The other co-authors reviewed and commented on the manuscript to improve the quality of the paper.

Publication V: "Design and Technical Evaluation of an Implantable Passive Sensor for Minimally Invasive Wireless Intracranial Pressure Monitoring" was published with the contribution of the authors and the co-authors. In this paper, the author conducted the experiments and wrote the manuscript. The other co-authors reviewed and commented on the manuscript to improve the quality of the paper.

2 Principle of inductively coupled LC-based passive sensors

2.1 Inductive telemetry using single turn external reader loop

The telemetry system paradigm for inductively coupled sensors includes an LC tank circuit, which is inductively coupled to an external reader loop. The electrical model of the system is depicted in Fig. 3. The sensor contains an inductive coil connected to a miniature capacitive (MEMS) pressure-sensing element.

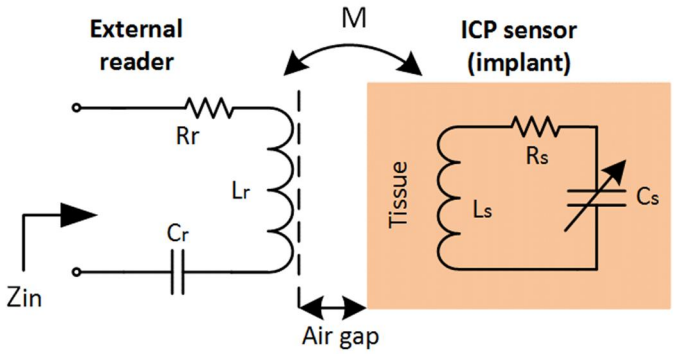

Fig. 3. Electrical model of the wireless telemetry system.

The inductance of the coil and the capacitance of MEMS pressure sensor create an LC oscillator with a known resonance frequency, which is given by

$$f_s = \frac{1}{2\pi\sqrt{L_s C_s}} \tag{1}$$

where L_s , C_s and f_s are the inductance of the spiral coil, capacitance of the MEMS pressure sensor and resonance frequency of the LC tank circuit, respectively [I]. The resonance frequency of the LC circuit changes as a function of applied pressure. It should be noted that C_s is not the only capacitive contributor to the resonance frequency, as parasitic capacitance created by coating material and surrounding tissue affects the net capacitance. The impact of parasitic capacitance on the quality factor and resonance frequency is presented in Chapters 2 and 4. The wireless measurement is established through an inductive link. When the external reader loop is excited with an alternating current (AC), an electromagnetic (EM) field is created around the loop. If the LC sensor is in the near-field zone of the reader loop, the EM field around the reader loop induces a current in the sensor's coil proportional to the magnitude of the magnetic field. The current flow in the sensor side loop creates a secondary EM field around the sensor's coil, which impacts the

current flow in the external reader loop [I]. The resonance frequency of the sensor can be detected by measuring the input impedance of the reader antenna. Applying the mesh equations for each loop shown in Fig. 3, the input impedance is given by [56],[I]

$$Z_{in} = R_r + j\omega L_r + \frac{1}{j\omega C_r} - \frac{(j\omega M)^2}{j\omega L_s + \frac{1}{j\omega C_s} + R_s} \tag{2}$$

At resonance, where $L_r C_r = 1/4\pi^2 f_r^2$ and $L_s C_s = 1/4\pi^2 f_s^2$ and substituting $M = K\sqrt{L_r L_s}$, the input impedance can be expressed by [56], [I]

$$Z_{in} = R_r + j\omega L_r \times \left[1 - \left(\frac{f_r}{f}\right) + \frac{K^2 \left(\frac{f}{f_s}\right)^2}{1 - \left(\frac{f}{f_s}\right)^2 + \frac{jR_s}{\sqrt{\frac{L_s}{C_s}}}\left(\frac{f}{f_s}\right)}\right] \tag{3}$$

where f is the excitation frequency, f_r is the resonance frequency of the reader, and K is the coupling coefficient of the inductive link. In view of Eqs. (2) and (3), the input impedance (Z_{in}) varies as a function of change in the applied pressure, and the coupling strength depends on K, which is affected by several factors, including the distance between the coils, dielectric material, mutual alignment, geometric properties and ohmic losses of the coils [57]. When the frequency of excitation is equal to the resonance frequency of the sensor ($f = f_s$), the input impedance and the impedance phase of the reader loop can be expressed by [I]

$$Z_{in} = R_r + \omega L_r \frac{K^2}{R_s}\sqrt{\frac{L_s}{C_s}} + j\omega L_r \left[1 - \left(\frac{f_r}{f}\right)\right] \tag{4}$$

$$\angle Z_{in} = \tan^{-1}\left[\frac{X_{in}}{R_{in}}\right] = \tan^{-1}\left[\frac{\omega L_r \left[1 - \left(\frac{f_r}{f}\right)\right]}{R_r + \omega L_r \frac{K^2}{R_s}\sqrt{\frac{L_s}{C_s}}}\right] \tag{5}$$

where R_{in} and X_{in} are the resistive and reactive components of the input impedance, respectively. According to Eq. (5), any change in the capacitance of the MEMS sensor impacts the impedance phase, and thus, pressure variation can be detected by measuring the phase of the input impedance of the reader antenna.

As mentioned previously, the intracranial pressure is measured by detecting the resonance frequency of the sensor. In addition to the resonance frequency, the phase difference between the transmit and receive signals provides information on the pressure variation. The inductively

coupled sensor with reader antenna can be considered as a complex load at the end of a transmission line with characteristics impedance of Z_o. With this assumption, the reflection coefficient is defined as [I]

$$\Gamma = \frac{Z_{in} - Z_o}{Z_{in} + Z_o} = \frac{R_{in} + j\,X_{in} - Z_o}{R_{in} + j\,X_{in} + Z_o} \tag{6}$$

The reflection coefficient can be split into its real and imaginary parts and expressed by [I]

$$\Gamma = \frac{R_{in}^2 - Z_o^2 + X_{in}^2}{R_{in}^2 + X_{in}^2 + Z_o^2 + 2Z_o R_{in}} + j\,\frac{2Z_o X_{in}}{R_{in}^2 + X_{in}^2 + Z_o^2 + 2Z_o X_{in}} \tag{7}$$

Substitution of R_{in} and X_{in} from (4) in (7) yields [I]

$$\varphi = \tan^{-1}\left[\frac{Im\{\Gamma\}}{Re\,\{\Gamma\}}\right] = \tan^{-1}\left[\frac{2Z_o X_{in}}{R_{in}^2 + X_{in}^2 - Z_o^2}\right] \tag{8}$$

$$= \tan^{-1}\left[\frac{2Z_o \omega L_r\left[1 - \left(\frac{f_r}{f}\right)\right]}{\left(R_r + \omega L_r \frac{K^2}{R_s}\sqrt{\frac{L_s}{C_s}}\right)^2 + \left[\omega L_r\left[1 - \left(\frac{f_r}{f}\right)\right]\right]^2 - Z_o^2}\right] \tag{9}$$

In the telemetry model with single turn loop reader, the resonance frequency of the sensor, impedance-phase dip frequency and reflection phase of the load are measured as the responsive parameters to the pressure variations.

2.2 Inductive telemetry using a dual-port planar RF probe

Wireless interrogation of an LC implant using a single turn loop benefits from simplicity in design and analysis of the coupled system (as discussed in Section 2.1). However, isolation of the weak signal from a deep miniature implant is challenging, especially at high frequencies [58]. To overcome the limitations of the measurement using the single turn loop, Talman et al. [59] reported a dual loop orthogonal-coil RF probe to detect the resonance frequency of the LC-based implantable sensors. The proposed RF probe contains two separate orthogonally oriented loops for excitation of the sensor and collection of the received signal from the implant. The proposed geometry provides natural electromagnetic isolation between the transmit and receive loops (T/R isolation). The level of T/R isolation determines the sensitivity of the probe in the detection of the sensors. The RF probe proposed by Talman et al., could provide up to 90 dB T/R isolation within the frequency range of 1-100 MHz, which is adequate for detection of miniature implants. However, the RF probe, with an overall size of 250 x 250 x 65 mm^3, is not suitable for portable and wearable applications. An alternative to the 3D orthogonal-coil RF probe is the planar form

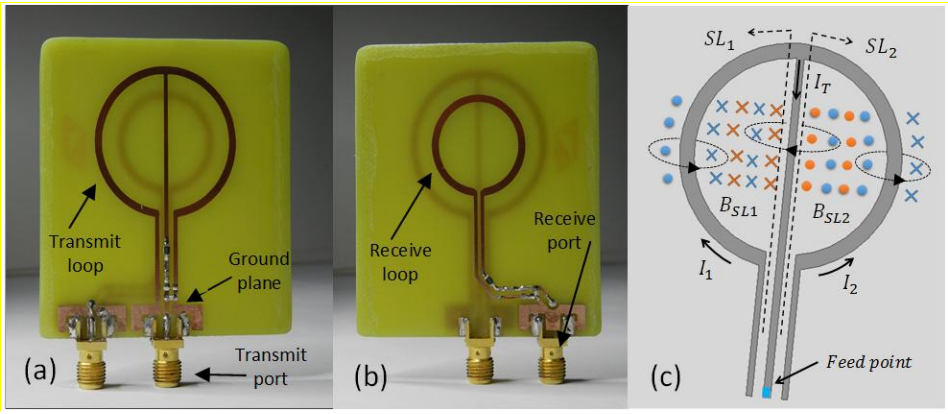

Fig. 4. Dual-port planar antenna. (a) Transmit loop. (b). Receive loop. (c) Graphical illustration of the magnetic fields around the transmit loop [II], © 2017 IEEE.

of the device. To this end, a dual-port planar antenna was designed as a compact, small form factor and portable version of the 3D RF probe. The geometry of the proposed planar antenna is shown in Fig. 4. It consists of separate transmit and receive channels for wireless interrogation of the LC-based sensor. The transmitter unit is a center-tap loop and the receiver is a single-turn loop. The transmit and receive loops are placed on the top and bottom layer of an FR4 substrate, respectively. The proposed antenna geometry provides electromagnetic isolation between the transmit and receive channels [II]. The principle of operation is explained in the following.

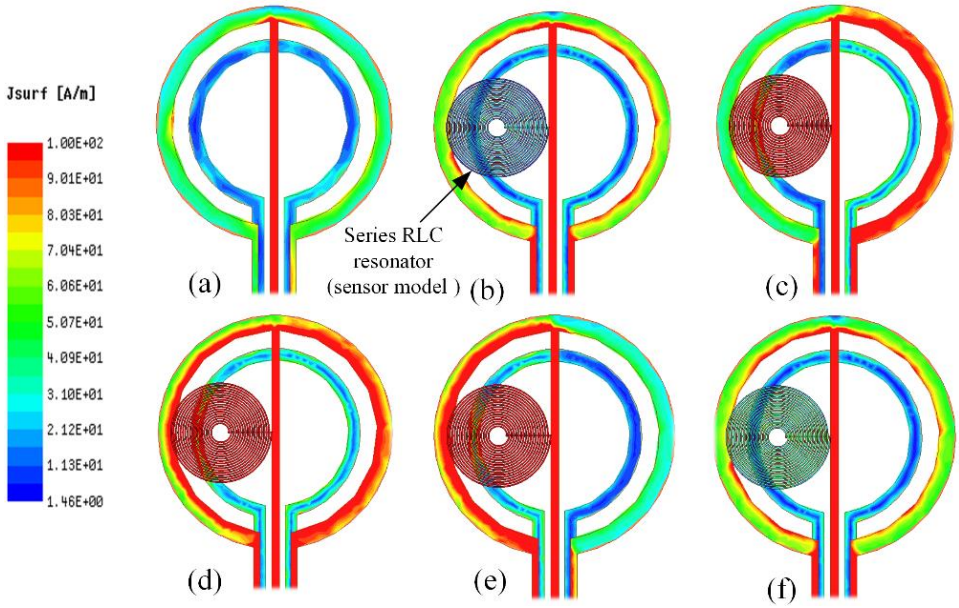

Fig. 5. Simulated current density in the planar antenna. (a) Unloaded antenna. (b) The sensor is coupled with SL_1 at: (b) frequencies far and below the resonance, (c) frequencies near and below the resonance, (d) the resonance frequency, (e) frequencies near and above the resonance, (f) frequencies far and above the resonance [II], © 2017 IEEE.

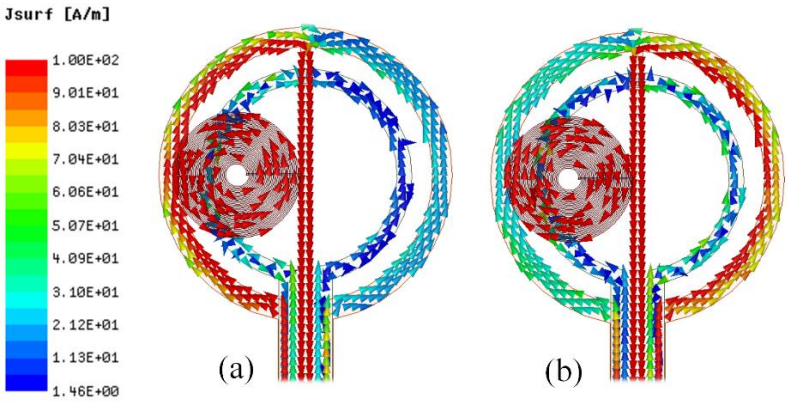

Fig. 6. Simulated current flow in the planar antenna and sensor's coil at frequencies (a) above the resonance, (b) below the resonance [II], © 2017 IEEE.

Excitation of the unloaded transmit loop through the feeding point (shown in Fig. 4(c)) creates a symmetric pattern of opposing magnetic fields around the semicircular loops (SL_1 and SL_2) as shown in the same figure. Each opposing magnetic field induces a current in the receive loop proportional to the magnitude of the corresponding magnetic field. Since the opposing magnetic fields are symmetric, the magnitude of the included currents is equal and opposing. Thus, the resultant induced current in the receive loop is zero, meaning that no power is transmitted from the transmit loop to the receive loop, and the loops remain decoupled. In order to measure the resonance frequency of the sensor, the LC sensor should be placed in the near-field zone of the antenna and centrally aligned to either of the semicircular loops. In this analysis, we assume that the LC sensor is aligned and coupled to SL_1. When the LC sensor is coupled with SL_1, the impedance of the sensor is reflected into the same semicircular loop. Thus, the impedance of SL_1 becomes higher than the impedance of SL_2 , and consequently, a greater amount of current passes through SL_2. Unequal current flow in the semicircular loops cancels the symmetry of the opposing magnetic fields. Therefore, a current proportional to the magnitude of the resultant magnetic fields around the semicircular loops is induced to the receive loop [II].

In order to further investigate the behavior of the planar antenna, a comprehensive electromagnetic simulation was conducted using ANSYS HFSS. The simulated current density (complex magnitude) in the planar antenna is shown in Fig. 5 (a-f). As can be seen from Fig. 5(a), in the absence of the sensor, the induced current in the receive loop is extremely insignificant compared to the excitation current. When the sensor is coupled with SL_1, the current density in SL_2 and the receive loop increase, as the frequency of the excitation approaches the resonance frequency of the sensor (shown in Fig. 5(b,c)). At frequencies above the resonance frequency, direction of the current flow in the sensor undergoes a 180 degree phase change (shown in Figs. 6 (a,b)). This reverses the loading effect on SL_1, meaning that at frequencies above the resonance, the impedance of SL_1 becomes less than the impedance of SL_2, and consequently, a greater amount of current flows through SL_1 (shown in Fig. 5(f)). Recalling that in a series RLC circuit, the current reaches its maximum at resonance [60] (shown in Fig. 5(d)), where the capacitive reactance and inductive reactance cancel each other out and current phase oscillates between −90°

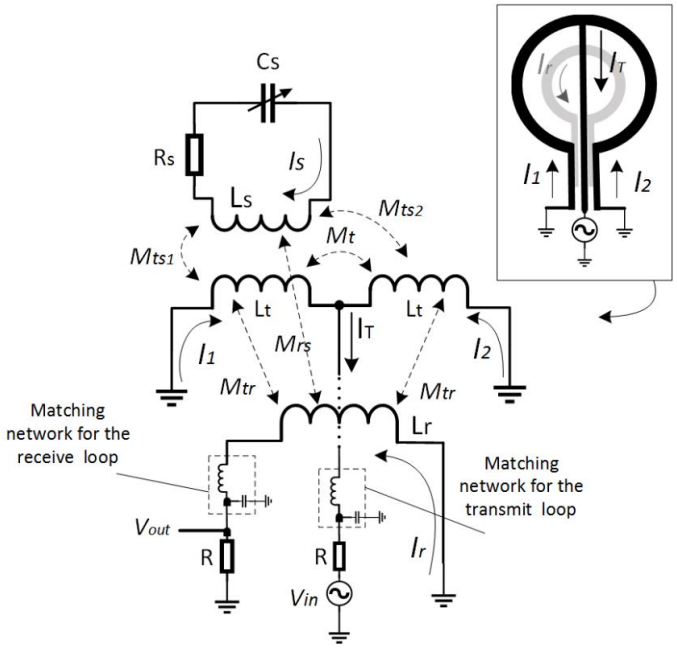

Fig. 7. The electrical model of the planar antenna [II], © 2017 IEEE.

and +90°. Therefore at the resonance frequency, the receive loop receives the maximum induced current where loading effect on SL_1 and SL_2 is exchanged periodically. The electrical model (equivalent circuit) of the antenna is illustrated in Fig. 7. The current in each loop can be calculated through the following mesh equations:

$$j\omega L_t I_1 + j\omega M_t I_2 + (I_1 + I_2)R + V_{in} + j\omega M_{ts1} I_s - j\omega M_{tr} I_r = 0 \quad (10)$$

$$j\omega M_t I_1 + j\omega L_t I_2 + (I_1 + I_2)R + V_{in} + j\omega M_{ts2} I_s + j\omega M_{tr} I_r = 0 \quad (11)$$

$$j\omega M_{ts1} I_1 + j\omega M_{ts2} I_2 + I_s R_s + \frac{I_s}{j\omega C_s} + j\omega L_s I_s - j\omega M_{rs} I_r = 0 \quad (12)$$

$$-j\omega M_{tr} I_1 + j\omega M_{tr} I_2 - j\omega M_{rs} I_s + j\omega L_r I_r + I_r R = 0 \quad (13)$$

The mesh equations can be summarized by the following matrix [II]:

$$\begin{bmatrix} I_1 \\ I_2 \\ I_s \\ I_r \end{bmatrix} = j\omega \begin{bmatrix} \left(L_t + \frac{R}{j\omega}\right) & \left(M_t + \frac{R}{j\omega}\right) & M_{ts1} & -M_{tr} \\ \left(M_t + \frac{R}{j\omega}\right) & \left(L_t + \frac{R}{j\omega}\right) & M_{ts2} & M_{tr} \\ M_{ts1} & M_{ts2} & \left(L_s - \frac{1}{\omega^2 C_s} + \frac{R_s}{j\omega}\right) & -M_{rs} \\ -M_{tr} & M_{tr} & -M_{rs} & \left(L_r + \frac{R}{j\omega}\right) \end{bmatrix}^{-1} \times \begin{bmatrix} -V_{in} \\ -V_{in} \\ 0 \\ 0 \end{bmatrix} \quad (14)$$

where V_{in} and V_{out} are the source and induced voltage (in the receive loop), respectively. I_s denotes the current in the sensor, and I_r is the induced current in the receive loop. R represents a 50-ohm resistor (source and load impedances). C_s is the capacitance of the MEMS pressure sensor. Inductance and resistance of the inductive coil are denoted by L_s and R_s.The inductances of each semicircular loops and the receive loop are denoted by L_t and L_r , respectively. M_{tr} denotes the mutual inductance between each semicircular loop and the receive loop. M_{ts1}, M_{ts2} are the mutual inductances between the sensor and the SL_1 and SL_2, respectively. M_{rs} is the mutual inductance between the receive loop and sensor, and M_t denotes the mutual inductance between SL_1 and SL_2.By solving the above 4×4 matrix in Eq. (14), the induced current and voltage in the receive loop are expressed by [II]

$$I_r = \frac{j\omega I_s[M_{tr}(M_{ts1} - M_{ts2}) + M_{rs}(M_t - L_t)]}{(j\omega L_r + R)(M_t - L_t) + 2j\omega M_{tr}^2} \tag{15}$$

$$V_{out} = \frac{j\omega I_s[M_{tr}(M_{ts1} - M_{ts2}) + M_{rs}(M_t - L_t)]\,R}{(j\omega L_r + R)(M_t - L_t) + 2j\omega M_{tr}^2} \tag{16}$$

$$|V_{out}| = \frac{I_s[M_{tr}(M_{ts1} - M_{ts2}) + M_{rs}(M_t - L_t)]\,R}{\sqrt{[L_r(M_t - L_t) + 2M_{tr}^2]^2 + \left[\frac{R_0(M_t - L_t)}{\omega}\right]^2}}. \tag{17}$$

As Eq. (17) states, $|V_{out}|$ is maximized when I_s reaches the maximum value. Recalling that in a series RLC resonator, the current peaks at the resonance frequency [60] with a stable voltage source (V_{in}), $|V_{out}/V_{in}|$ reaches the maximum value at the resonance frequency of the sensor. Thus, the resonance frequency of the sensor can be measured by measuring the forward transmission gain (S_{21} parameter) between the transmitter and receiver [II].

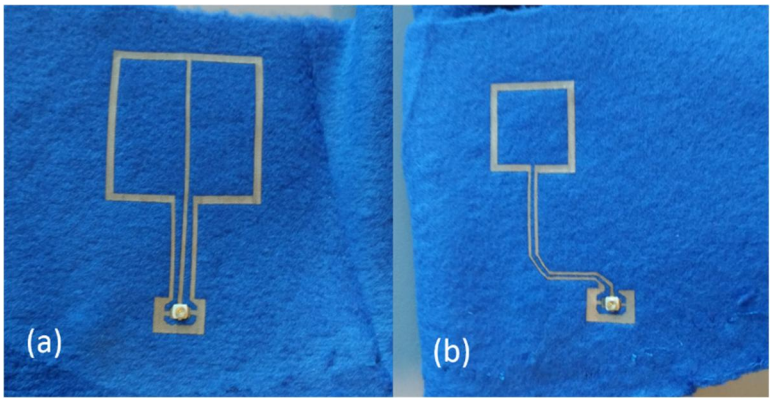

Fig. 8. Wearable dual-port planar antenna. (a) Transmit loop. (b) Receive loop. The ultra-miniature coaxial connector (UMCC) is attached to the textile fabric using silver conductive epoxy adhesive.

2.2.1 Wearable planar antenna

In real-life applications, there might be scenarios in which continuous ICP monitoring may require wearable electronics to be worn by a patient. To this end, a wearable version of the antenna was fabricated using conductive fabric (shown in Fig. 8). In the wearable version of the antenna, the same antenna topology was implemented; however, instead of the circular loops rectangular loops were used. The rectangular loops were formed by laser cutting the geometry of the loops from a conductive fabric. The conductive fabric is heat sensitive and can stick to textile substrates using thermal compression. The proposed wearable antenna could provide at least 50 dB T/R isolation within the frequency range of 1-100 MHz.

2.3 3D version of the planar antenna

The 3D version of the planar antenna is the volumized version of the 2D antenna with the same geometry. The 3D antenna was fabricated by laser cutting the frame of the transmit and receive loops from an FR4 substrate, then, the whole volume of the frame was covered by adhesive copper tape. The transmit and receive loops are placed on a cardboard using a sticky deformable paste (Blu-Tack) and separated by 1.6 mm. A prototype of the antenna is shown in Fig. 9 [II].

As mentioned in the theoretical analysis of the antenna performance, the level of T/R isolation highly depends on the symmetry of the antenna. In fact, fabrication of a perfect symmetric antenna is essential to achieve the best possible T/R isolation. More specifically, in order to create a perfect symmetric opposing magnetic field, the current flowing in semi-circular loops should be exactly equal. This requires an ideal impedance balance between the SL_1 and SL_2. However, in practice, the fabrication process might distort the impedance balance, and thereby, unequal opposing magnetic fields are created around the semi-circular loops. This will result in power transmission from transmitter to receiver. In order to mitigate this issue in the 3D antenna, the transmit loop can slightly rotate around z-axis to adjust the T/R isolation. The effective angular rotation to tune the T/R isolation found to be less than ±1 degree [II].

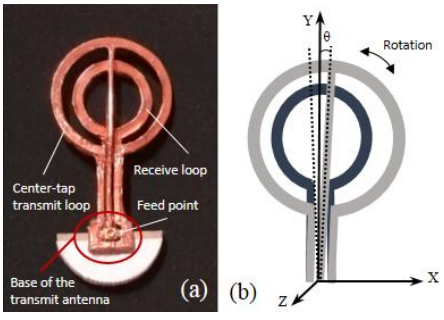

Fig. 9. (a) 3D version of the dual-port antenna. (b) Angular rotation of the transmit antenna [II], © 2017 IEEE.

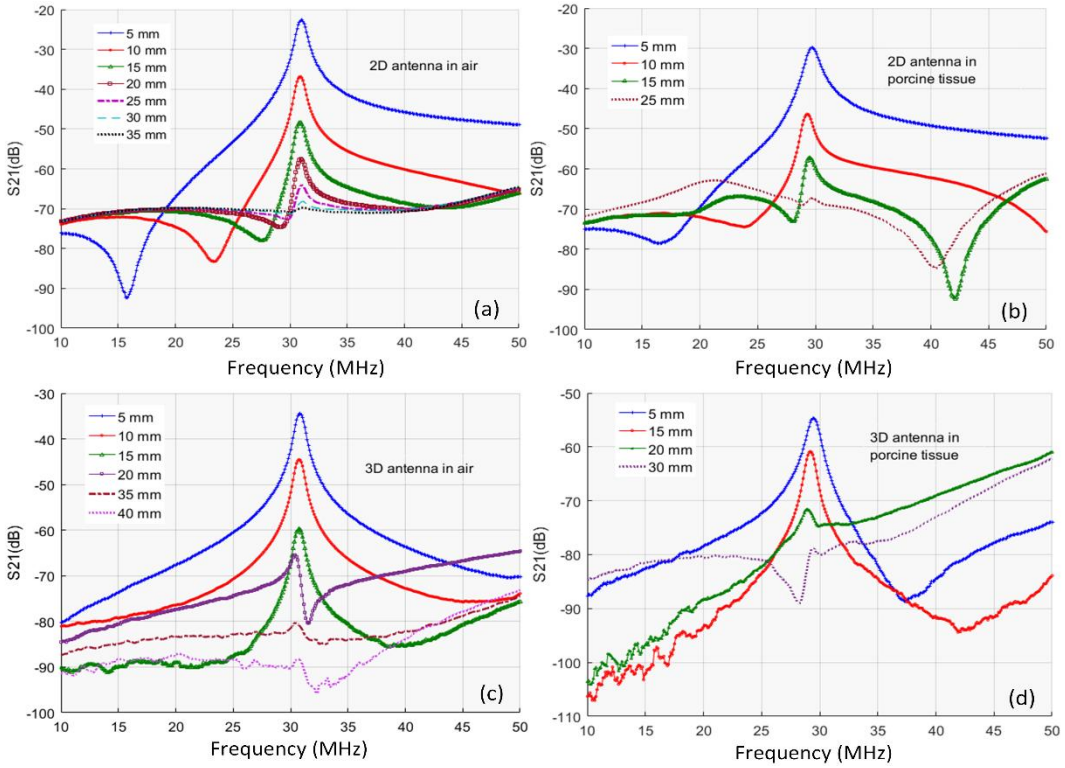

Fig. 10. The measured resonance frequency of the sensor. (a) With 2D antenna in air. (b) With 2D antenna in porcine tissue. (c) With 3D antenna in air. (d) With 3D antenna in porcine tissue [II], © 2017 IEEE.

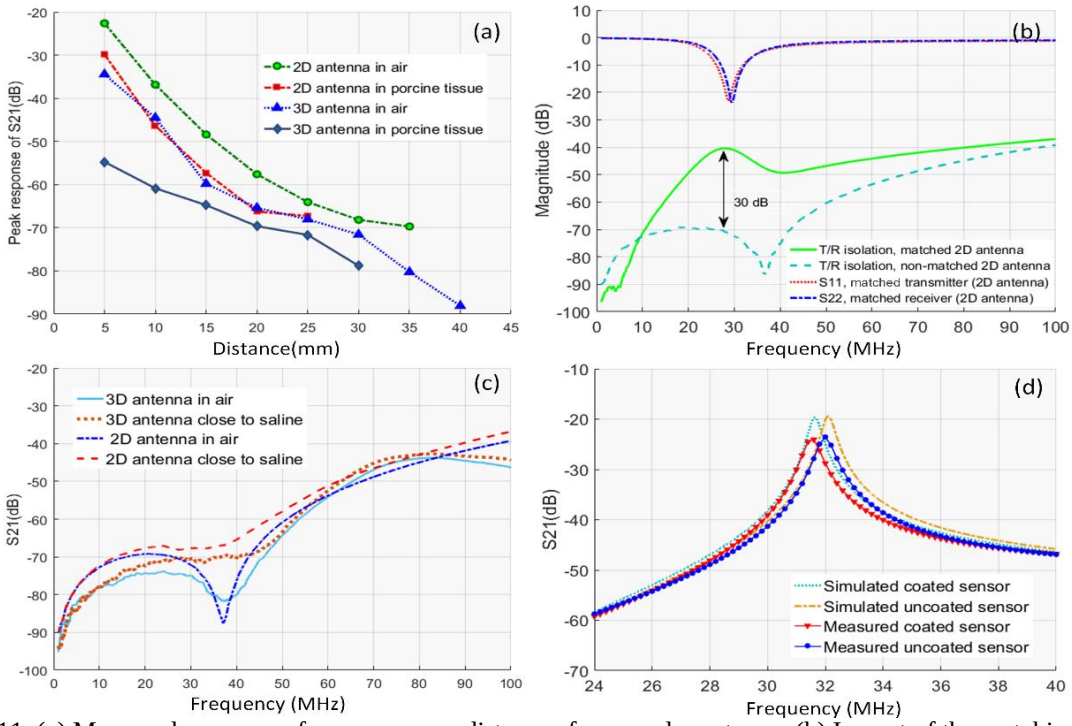

Fig. 11. (a) Measured resonance frequency over distances from reader antenna. (b) Impact of the matching network on T/R isolation. (c) T/R isolation of the antenna near the saline tank. (d) Impact of coating on the resonance frequency [II], © 2017 IEEE.

2.4 Measurement with the planar RF probe

The performance of the RF probe was verified in air and porcine tissue (shown in Fig. 10(a-d)). The porcine tissue was used to emulate the dielectric properties of the human tissue. In the measurement in air, the resonance frequency of the sensor was measured over several distances from the planar antenna. The distance between the sensor and antenna was increased at 5-mm intervals. For measurement in the porcine tissue, first, the sensor was coated with silicon adhesive (ε_r=2.66, tan δ=0.007) and then placed inside the tissue at different depths through a small incision. The coating layer slightly reduced the resonance frequency (< 1 MHz) due to the additional parasitic capacitance (shown in Fig. 11(d)). Analogous to the measurement in air, the distance between the antenna and the sensor was increased at 5-mm intervals. The measured resonance frequency with 2D and 3D antennas is shown in Fig. 11 (a). As can be seen from the figure, with the 2D antenna, the resonance frequency of the sensor could be detected when the sensor is placed as far as 35 mm in air and 25 mm in porcine tissue. In the measurement with the 3D antenna, the detection range extended up to 40 mm in air and 30 mm in porcine tissue. The experiment results suggest that the 3D antenna could provide extended detection range compared to the 2D antenna. This can be explained by the improved T/R isolation of the 3D antenna through the tuning functionality [II]. Moreover, its 3D structure benefits from an enhanced effective coupling area for the inductive link between the antenna and sensor [61].

The impact of the matching circuit on the T/R isolation was investigated by matching both transmit and the receive loops around the resonance frequency of the sensor. As shown in Fig. 11(b), matching the loops degrades the T/R isolation, more severely around the matching frequency. Since highly isolated transmit and receive loops are required for the detection of an implant in deep, the T/R isolation was measured as close as 1 mm to a saline container to ensure that the eddy current does not degrade the T/R isolation in real-life applications. As illustrated in Fig. 11 (c), the eddy current has an insignificant impact on the antenna performance.

2.5 Design Consideration for an LC implant

As mentioned previously, the design of an implant for measuring a specific parameter inside the body requires careful consideration of the nature of the parameter to be measured (e.g. temperature, pressure, strain etc.) as well as the location of the implantation and properties of the tissue surrounding the sensor when implanted. A key consideration in the design of the LC sensor is to ensure that the sensor is easily detectable when implanted at the desired depth inside the tissue. In addition, the size of the implant should be kept as small as possible to provide minimally invasive implantation. To this end, the efficiency of the inductive link between the external reader and the sensor should be optimal while considering that geometric properties of the implant need to be as miniature as possible.

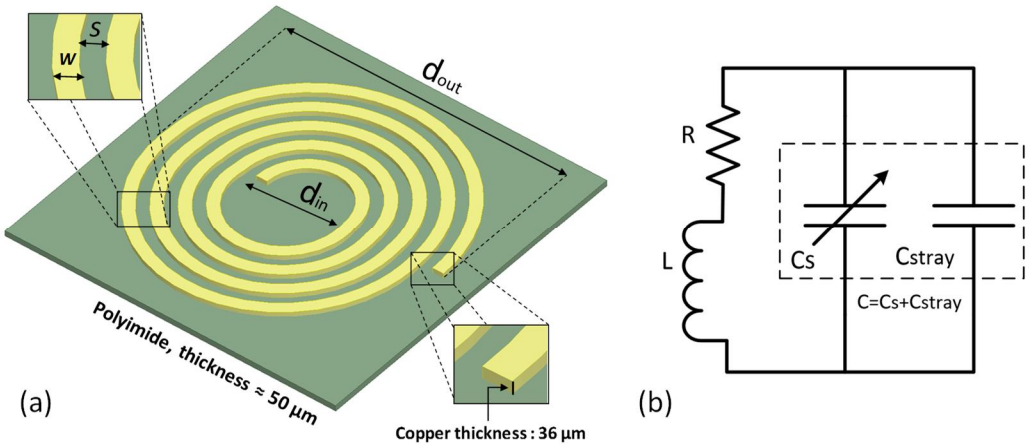

Fig. 12. (a) Geometric parameters of the planar spiral coil. (b) Equivalent circuit of the RLC sensor.

2.5.1 Implant size

The constraints on the size of the implant depend on the application of the implant and the organ in which the device is implanted. In most of the applications, a small form factor is required to provide minimally invasive implantation and patient comfort. Miniaturization is most critical in some specific applications, such as IOP monitoring and spinal implants, where devices as miniature as 2 mm and 4 mm are required, respectively [39], [62]. Basically, the overall size of the implant is dominated by the size of the planar inductor, which itself is interrelated to the inductance and quality factor of the LC resonator. In this study, the outer diameter of planar coils ranges from 13 to 22 mm. However, the sensor with outer diameter of the 13 mm has been used in the *in vivo* study.

2.5.2 Quality factor

An LC-based implant needs to achieve the sufficient Q factor to ensure that the sensor is detectable through near-field energy transfer between the implant and the external reader. Moreover, it should be sensitive enough to the variations of the quantity being measured [63]. However, maximizing the quality factor of the sensor might oppose the size and fabrication constraints. Therefore, there should be a tradeoff between the size, geometric properties and quality factor of the implant. In the following, a parametric analysis of the quality factor is discussed.

The quality factor of a series RLC resonant circuit (as modeled in Fig.12 (b)) for given resistance (R), inductance (L) and capacitance (C) is determined by

$$Q = \frac{1}{R}\sqrt{\frac{L}{C}} \tag{18}$$

The resistance of the of the spiral inductor has two components, DC resistance (R_{DC}) and frequency-dependent skin depth (δ), and can be estimated by [63]

$$R = R_{DC}\frac{T}{\delta}\frac{1}{1-e^{-T/\delta}} = \frac{1}{\sigma w\delta(1-e^{-\frac{T}{\delta}})} \tag{19}$$

where T is the thickness (copper thickness), w is the trace width, and σ is conductivity of the coil. The accurate computation of the inductance of an arbitrary spiral coil is complicated and requires field solver[64], however, it can be approximated by [63]

$$L = \frac{\mu_0 N^2(d_{in} + d_{out})}{4}\left[ln\frac{2.46}{p} + 0.20p^2\right] \tag{20}$$

where μ_0 is the magnetic permeability, N denotes number of the turns, d_{in} and d_{out} represent the inner and outer diameter, respectively, and p is the fill factor of the coil, which is defined as [63]

$$p = \frac{(d_{out} - d_{in})}{(d_{out} + d_{in})} = \frac{(2N+1)w + (2N-1)s}{2d_{out} - (2N+1)w - (2N+1)s}\ . \tag{21}$$

The capacitance of the RLC sensor is the sum of capacitance of the MEMS sensor (C_s) and parasitic capacitance (C_{stray}). There are several factors contributing to the creation of the parasitic capacitance, including coating of the spiral inductor, capacitance between adjacent traces and permittivity of the surrounding tissue when the sensor is implanted. According to the model shown in Fig. 12(b), the total capacitance (C) can be expressed by

$$C = C_s + C_{stray}\ . \tag{22}$$

For the implantable RLC sensor, the major contributors to the parasitic capacitance, and consequently to the quality factor, are the coating material, thickness of the coating layer and dielectric properties of the tissue. The MEMS pressure sensor (Murata SCB10H-B012FB) used in this study also shows considerable lossy behaviour at frequency above 50 MHz, which is discussed later in the following section. A detailed analysis on the impact of the parasitic capacitance on the ICP measurement is presented in Chapter 4.

A comprehensive parametric analysis of the quality factor based on the aforementioned equations is given in [63]. According to the study, the quality factor rises as d_{out} increases and reduces as the spacing between the turns increases. Therefore, the quality factor can be enhanced by setting those parameters to their limits, that is, maximizing the outer diameter and minimizing the spacing. However, in practice, the limits are set by the design concept (e.g. size and geometry) and fabrication constrains. In this study, spacing and trace width were set to150 ㎜ due to the manufacturing limits of the planar coil on a flexible polyimide substrate (thickness: 50 μm). The outer and inner diameters vary in different implementation of the spiral inductor. Table 1 presents geometric properties of the spiral inductors and the measured quality factor. For evaluation of the

Table 1. Geometric parameters of the fabricated spiral coils and measured Q factor.

Geometry of the inductor	Trace width/ Spacing [μm]	Inner diameter [mm]	Outer Diameter [mm]	Resonance frequency in air [MHz]	Number of turns [*N*]	Measured Q factor
Circular	150/150	4	22	13	30	62
Circular	150/150	2	15	29.5	20	61
Circular	150/150	4	13	35.3	15	60
Rectangular	150/150	1	15	30.9	20	60

quality factor, all the inductors were connected to 10 pF-capacitor and interrogated wirelessly through the dual-port planar antenna. The quality factor was extracted by measuring the 3-dB bandwidth of the peak response of the S_{21} parameter.

2.6 Sensitivity of the sensor

For the proposed LC sensor, the measurement sensitivity of the pressure variation is defined as the rate of change in the frequency shift of the sensor, with respect to the variation of the capacitance of the MEMS sensor. Considering that the MEMS sensor's capacitance changes as a function of the imposed pressure, the measurement sensitivity can be expressed by [57]

$$\frac{\partial f_s}{\partial C_s} = -\frac{1}{4\pi\sqrt{L_s C_s}} = -\frac{f_s}{2C_s}. \tag{24}$$

It can be interpreted from Eq. (24) that the sensitivity (pressure-depended frequency shift) increases, if the sensor is excited at a higher frequency. In addition, miniaturization of the implant is achievable at a higher excitation frequency by reducing the number of the spiral coil's turns. However, through empirical experiments, the MEMS sensor was found to introduce noticeable parasitic above 50 MHz, and consequently, the quality factor of the RLC resonator reduces. This imposes operating at lower frequencies. A comparative study on the impact of operation frequency on the sensitivity of the pressure measurement is presented in Chapter 4.

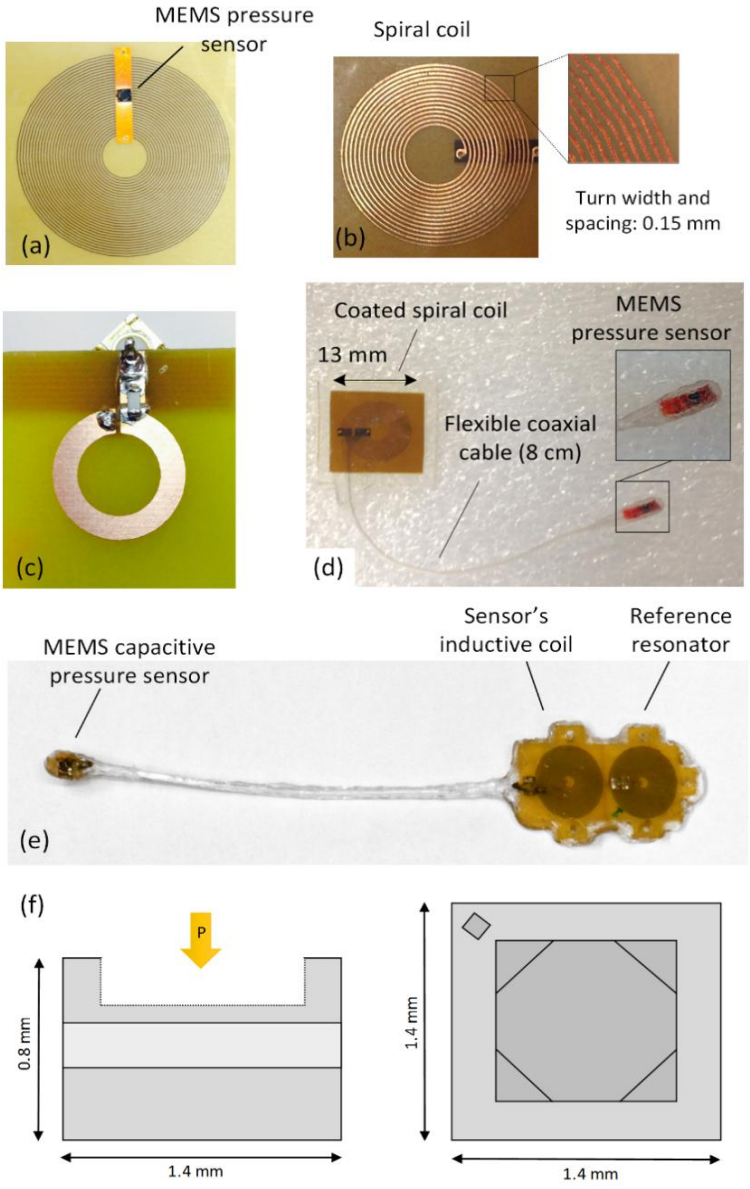

Fig. 13. Passive LC sensors designed in this study. (a) Sensor A, (b) Sensor B [I], (c) Single-turn reader antenna [I], (d) Sensor C [III]. (e) Dual-coil ICP sensor (Sensor M1). (f) The MEMS pressure sensor (cross-sectional and top views).

2.6.1 Specifications of the sensors

In this study, several sensors were designed with different specifications in terms of size, geometry, form factor and operation frequency. All the designed sensors follow the classic paradigm of an LC tank circuit, but were customized for different modes of ICP measurement. The specifications of each sensor are presented in Table 2, and the sensors are shown in Fig. 13. Each type of sensor has a unique label, as presented in the table (the reference tags are recalled in

Chapters 4 and 5). As mentioned previously, the inductive coil is connected to a variable MEMS capacitor to create a resonance at a specified frequency at air pressure. The capacitance of the pressure sensitive element varies as a function of the applied pressure, and thus, changing the resonance frequency of the LC tank. A graphical illustration of the MEMS sensor is shown in Fig. 13(f). In the proposed wireless telemetry, the inductive coil is placed on the skull and connected to the subdural MEMS sensor through an ultra-thin coaxial cable. In this way, the wireless channel between the implant and the external reader is shortened to reduce the length of the wireless channel, thereby improving the efficiency of the RF inductive link.

Table 2. Characteristics of the sensors used in this study.

Label in the corresponding study	Corresponding study	Resonance frequency in air [MHz]	Number of turns [*N*]	Diameter/trace width [mm]
A	*In vitro* (subdural)	13	30	22/0.15
B	*In vitro* (subdural)	31.2	15	13/0.15
C1, C2, C3	*In vitro* (intraparenchymal and intraventricular), Drift measurement	25	15	15/0.15
M1,T1,T2	*In vivo*	See Table 3 (page 38)	20	15/0.15

3 External ICP reader device

3.1 Reader electronics

Clinical utilization of the fully passive sensors requires a reader device for communication with the implant to readout the pressure value. To this end, a dedicated hand-held reader device was developed to communicate with the implant and record the ICP value. The functional block diagram of the reader device is shown in Fig. 14. The reader device is a Bluetooth-enabled device for wireless interrogation of the implant on demand. In order words, the pressure values can be read only when the reader device excites the implant and collects the received signal from the sensor. The measurement board comprises 4 major functional blocks including RF front-end, processor unit, wireless interface and power management unit. The RF front-end consists of separate transmit and receive channels. In the transmit channel, a programmable Direct Digital Synthesis (DDS, AD9951 [65]) generates a continuous wave (CW) RF signal to excite the implant. The bandwidth of the sweep frequency can be programmed by the user based on the resonance frequency of the sensor. The RF signal is transmitted to and received from the sensor via the dual port planar antenna. Through the receive channel, the received signal is amplified, filtered and then fed to an RF gain/phase comparator block (AD8302[66]). The RF gain/phase block compares the magnitude ratio of and the phase difference between the transmitted and received signals and produces DC output signals proportional to the magnitude ratio of and the phase difference between the transmitted and received signals.

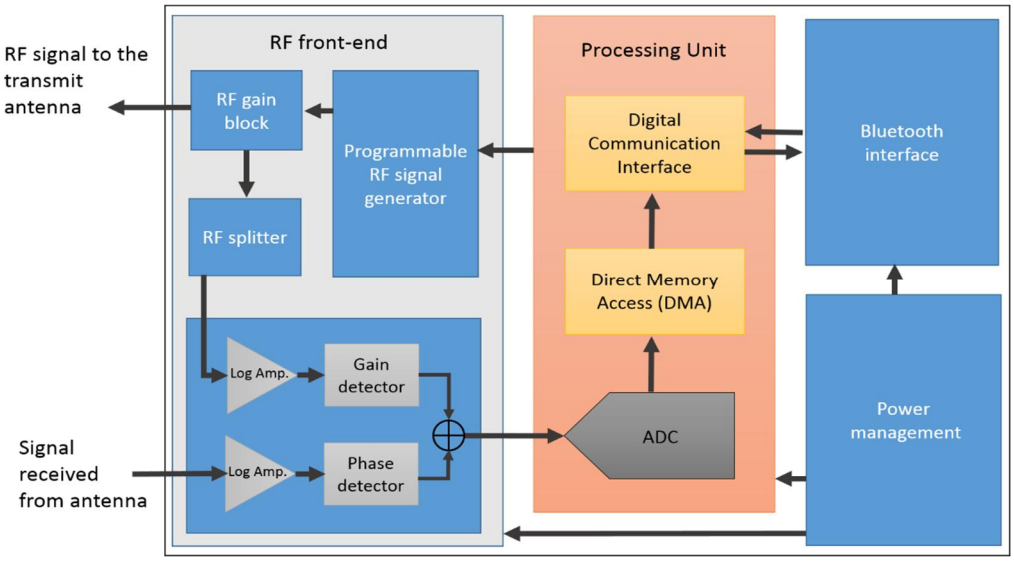

Fig. 14. Functional block diagram of the reader electronics.

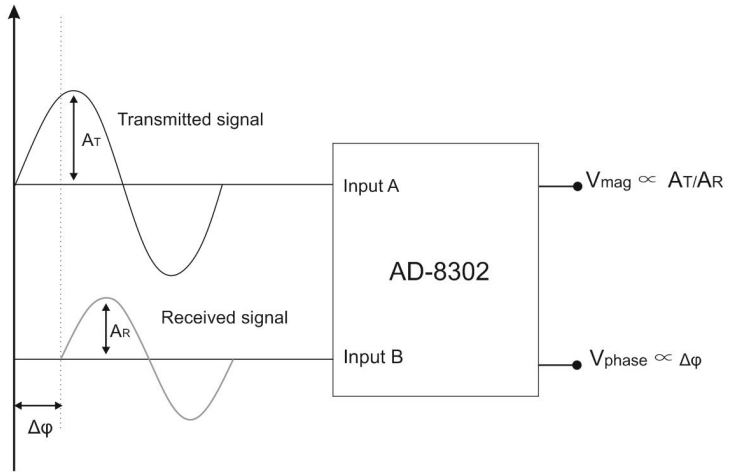

Fig. 15. AD8302 compares the magnitude ratio of and phase difference between the transmitted and received signals.

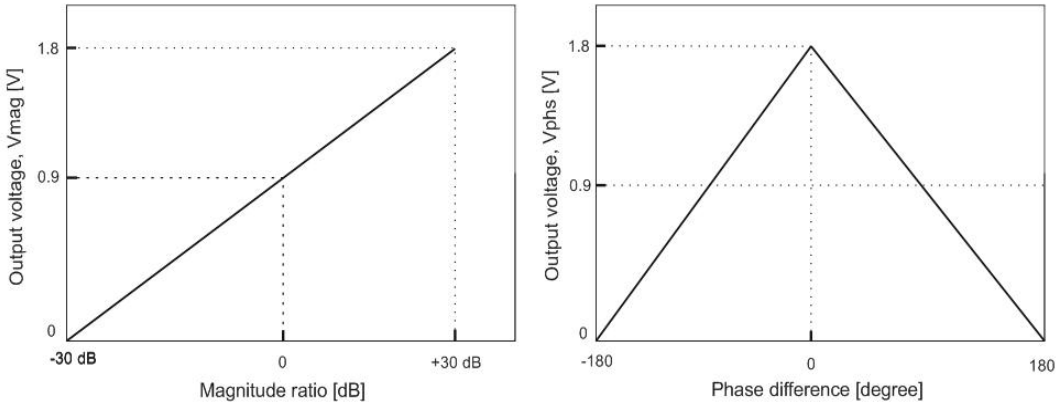

Fig. 16. DC output characteristics of the RF gain/phase comparator. Redrawn from [66].

The characteristics of the RF gain/phase comparator is shown in Figs. 15 and 16. As can be seen from the figures, the output voltage of the chip increases, as the magnitude ratio between the transmit and receive signals increases. In addition, the DC output voltage corresponding to the phase difference between the signals varies depending on whether the phase difference increases or declines. The input signals, that are transmitted and received, are captured by a cascade of matched demodulating logarithmic amplifiers. The output voltages generated by AD8302 are converted to digital values using a 16-bit delta-sigma analog to digital converter (ADC). A high performance embedded microcontroller (TI-MSP430F5529 [67]) captures the output digital data and transmits the data to a wireless Bluetooth module. The Bluetooth module is connected to a host PC via Bluetooth link for real–time transmission of the data. The incoming data stream to the PC is handled via a dedicated LabVIEW application. The application retrieves the incoming data and performs pre-processing for noise reduction. The application stores the ICP data, visualizes it and extracts the resonance frequency of the sensor from the frequency response.

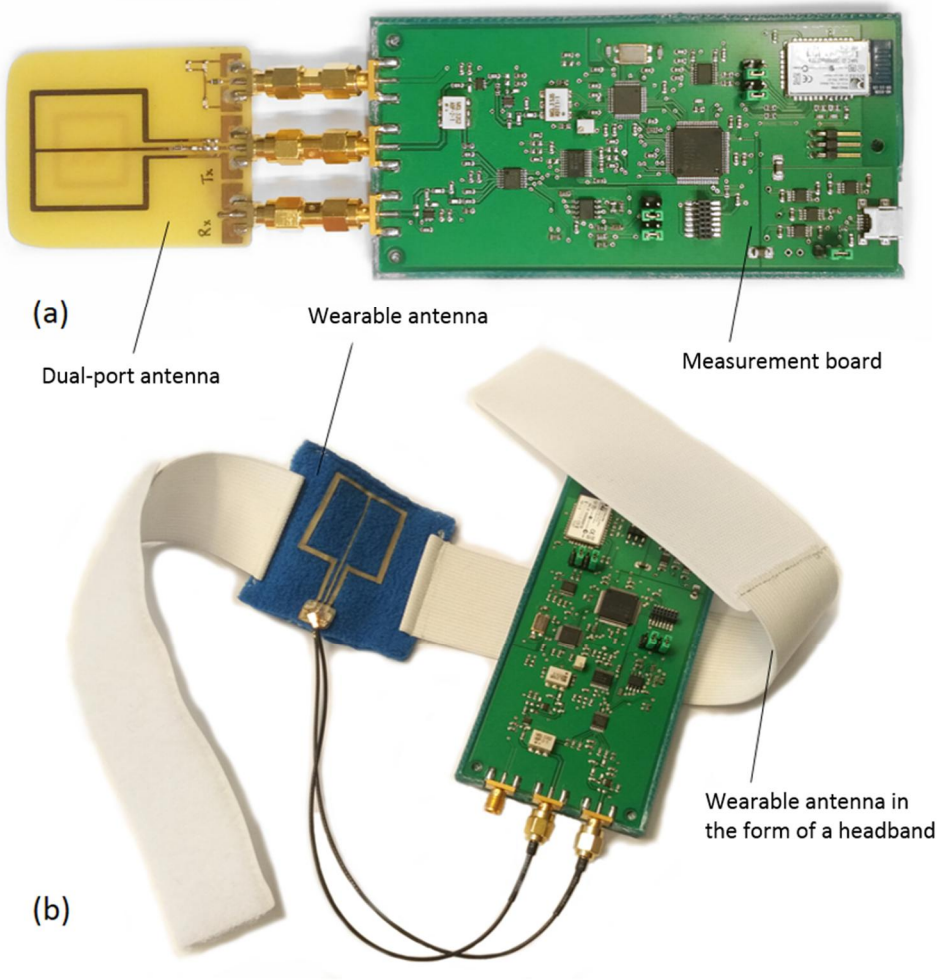

Fig. 17. Hand-held reader electronics for wireless communication with the ICP implant. (a) ICP reader with rigid dual-port antenna. (b) The wearable antenna is implemented in the form of a headband.

3.2 Software development

The software required for the reader device to perform the pre-defined tasks was developed in C programming language using IAR workbench IDE. The software first initiates the internal modules of the MCU, then, initializes the DDS signal generator and specifies the properties of the excitation signal including the bandwidth of the scan, phase offset and frequency of RF signal. The specific functions written in C handle the data communication between the microcontroller and the other modules of the measurement board.

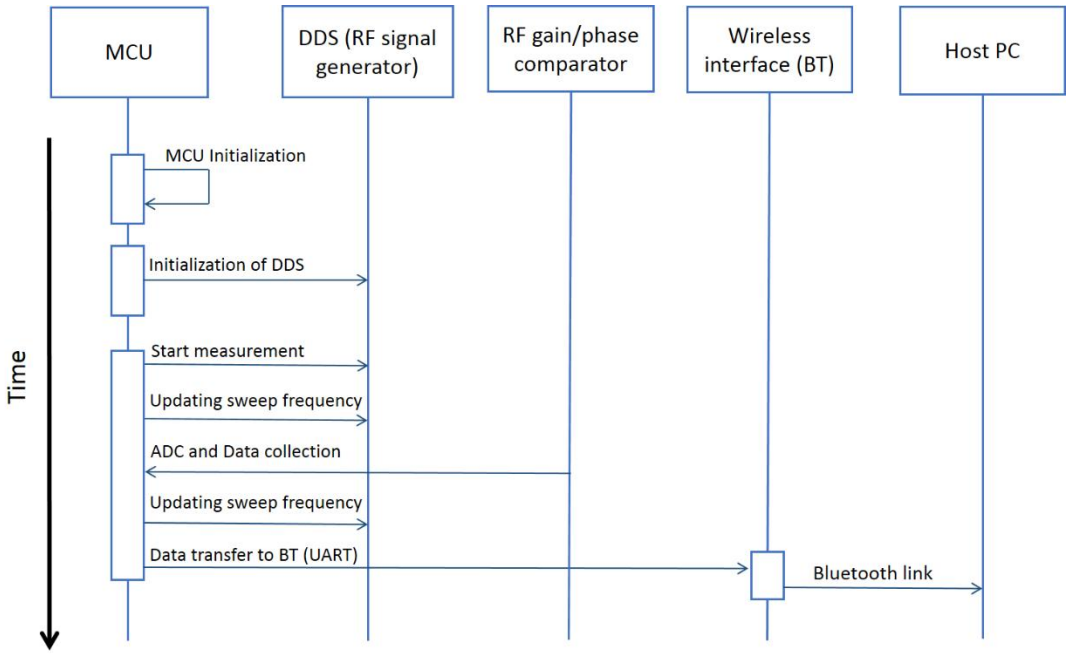

Fig. 18. Execution sequence of the program running on the reader's MCU.

As mentioned previously, a dedicated LabVIEW application was developed so that the measurement device interface with a PC in real-time. The developed application handles the incoming data from the measurement board and performs the necessary processing for detecting the resonance frequency.

3.3 Measurement with the ICP reader

As discussed earlier, the reader's electronics detect the resonance frequency of the sensor by measuring the magnitude ratio of and the phase difference between the transmit and receive signals. The planar antenna provides separate signal pathways for concurrent transmit and receive operation. The generated RF signal by DDS is split using an onboard 0-degree RF splitter. The splitter accepts the generated RF signal and outputs two RF signals with identical properties. As can be seen from Fig. 19, the generated RF signal is split into Output A and Output B. Output A is used to excite the implant, and Output B is used as the reference signal to be compared with the received signal.

The strength of the received signal depends on the distance between the sensor and the planar antenna. Thus, it is essential to keep the distance as short as possible. With implant topology discussed in Chapter 2, the coupling distance is shortened by placing the planar inductor under the skin and passing the pressure-sensing element to the subdural region through the coaxial cable.

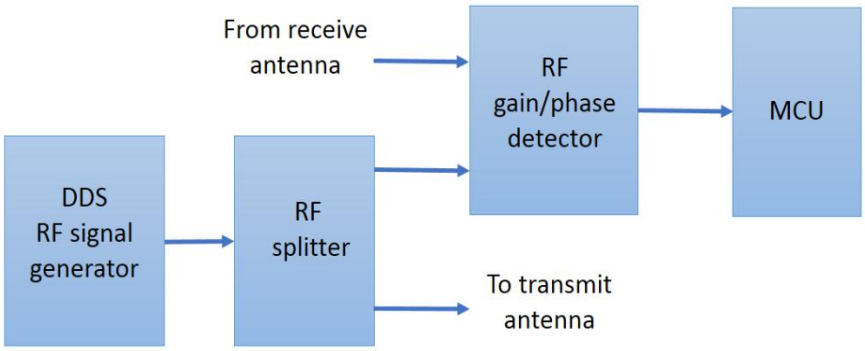

Fig. 19. The RF splitter outputs two identical signals.

The resonance frequency of the sensor is detected by searching for a peak in the frequency response of the sensor (Fig. 20(a)). In addition, as shown in Fig. 20 (b), the phase difference data shows a sharp dip almost at the resonance frequency of the sensor. The measured resonance frequency of a sample series RLC resonator (f_s=21.06 MHz) with the ICP reader and VNA is illustrated in Fig. 20.

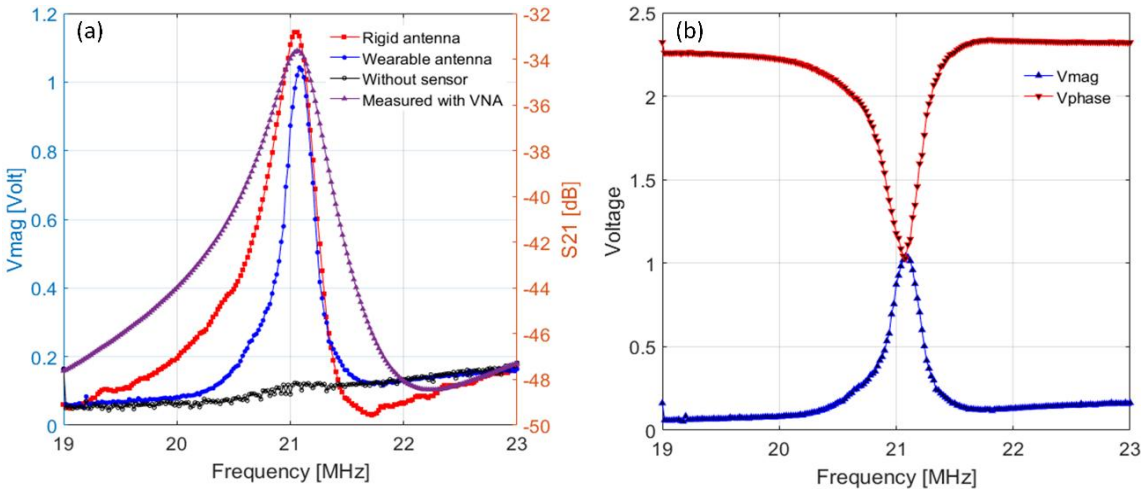

Fig. 20. (a) Resonance frequency of a sample RLC resonator measured with ICP reader and VNA. (b) Magnitude ratio of and phase difference between transmit and receive signals (data recorded by the ICP reader).

4 *In vitro* evaluation of the ICP sensor

The design of biomedical implants is carried out by advanced analysis of device performance through accurate modeling of the physiological condition using specific measurement setups. Further investigation may be done through *in vivo* studies using animal models and clinical trials. The following chapter reports the findings from simulation of different modes of ICP through specific measurement setups.

4.1 *In vitro* evaluation of subdural ICP monitoring

In order to assess the performance of the sensor for subdural ICP monitoring, a specific measurement setup was designed to emulate the subdural ICP measurement. As can be seen in Fig. 21, the measurement setup contains a water tank to create hydrostatic pressure, simulating the intracranial pressure. There are two valves to allow water intake and water drain. The sensor was placed at the bottom of the water tank, and the applied pressure was varied by changing the amount of water. The resonance frequency of the sensor was detected by measuring the input impedance of the external reader via a vector network analyzer (VNA), and the actual pressure was recorded using an industrial-grade pressure sensor (IMF electronic GmbH PA 3528 [68]). The gap between the reader and ICP sensor was filled with 5 mm of pig skin. In this measurement, two sensors (labeled as Sensor A and Sensor B in Table 2) with different resonance frequencies were used to study the impact of the operation frequency on the sensitivity of the measurement.

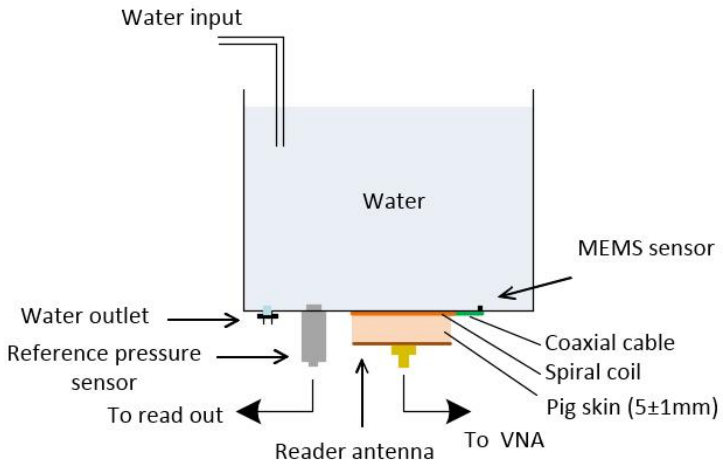

Fig. 21. Measurement setup for subdural ICP measurement [I]. The external reader used in the measurement is the single-turn reader shown in Fig.13 (c).

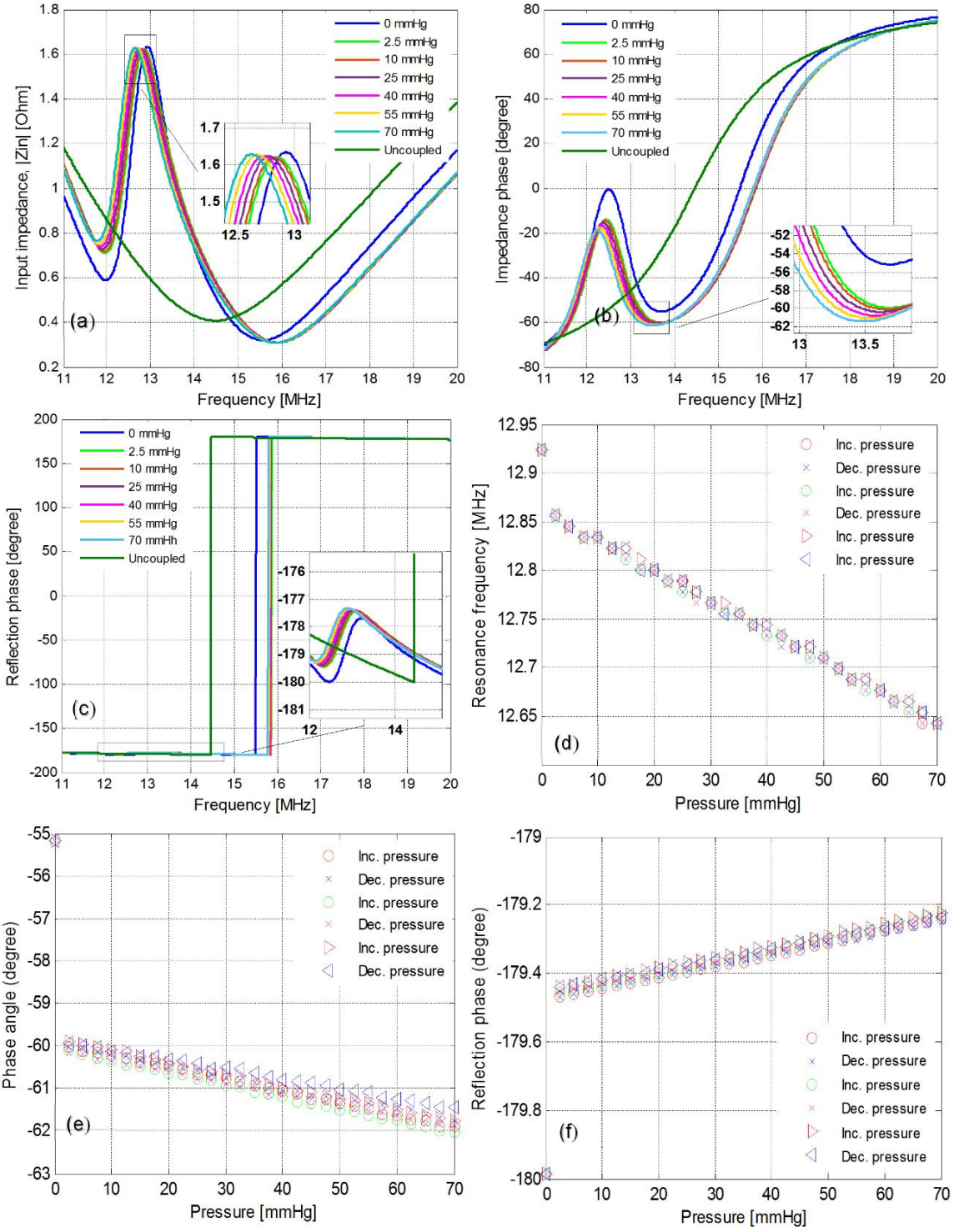

Fig. 22. Measurement data recorded from sensor A. (a) Magnitude and (b) phase angle of the input impedance. (c) Reflection phase. (d) Frequency shift versus the applied pressure. (e) Impedance phase dip. (f) Variation of the reflection phase as a function of the applied pressure [I].

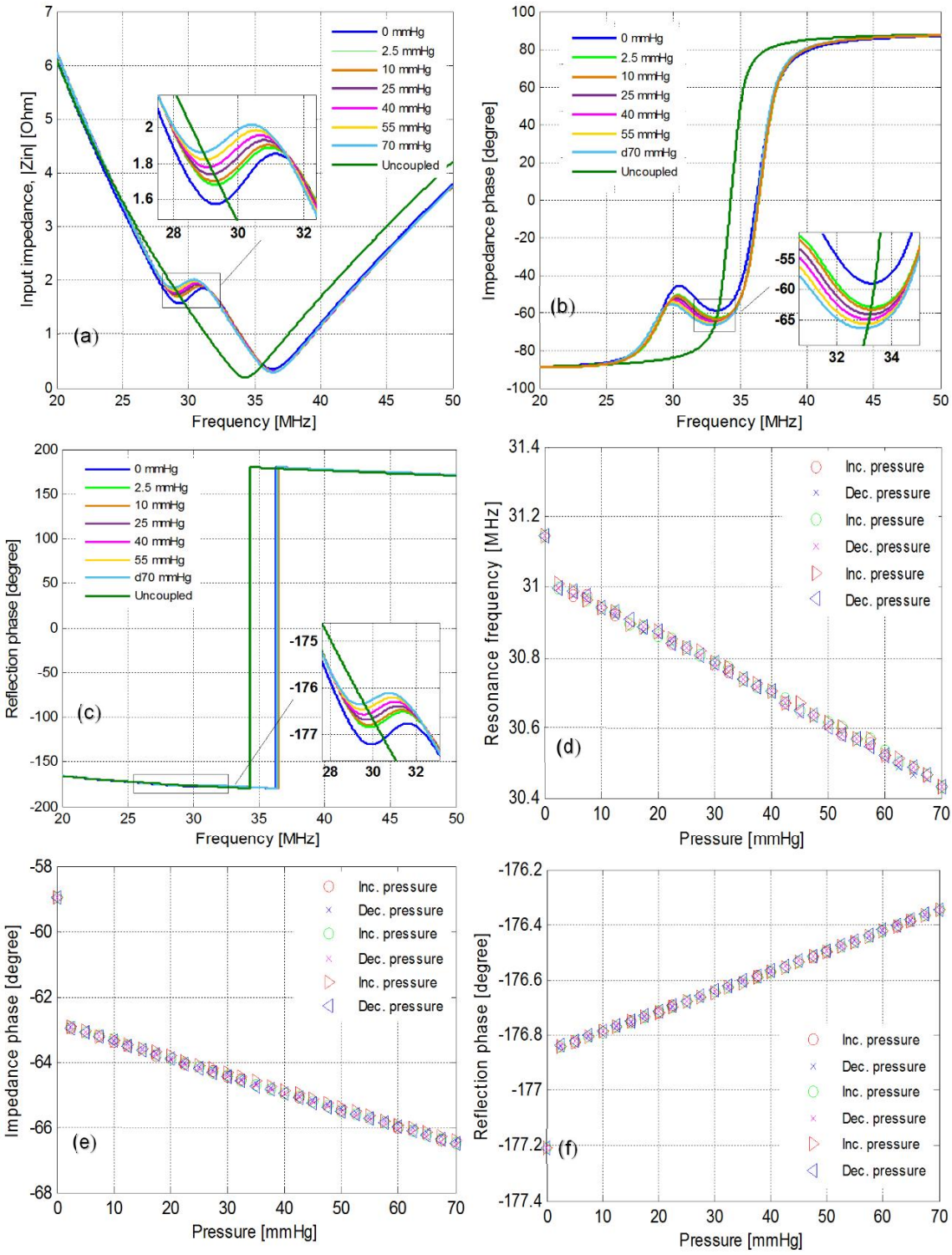

Fig. 23. Measurement data recorded from Sensor B. (a) Magnitude and (b) phase angle of the input impedance. (c) Reflection phase. (d) Frequency shift versus the applied pressure. (e) Impedance phase dip. (f) Variation of the reflection phase as a function of the applied pressure [I].

4.1.1 Findings from the *in vitro* subdural test

The measurement results from the subdural *in vitro* tests with Sensor A and B are shown in Figs. 22(a-f) and 23(a-f). As can be seen from the figures, the resonance frequency and impedance phase of the sensor varies as a function of the applied pressure and can be detected by measuring the magnitude and phase of the reader antenna's input impedance. In addition, measuring the phase of the reflection coefficient of the reader antenna could provide information on pressure variation, as explained in Chapter 2. In both measurements (with Sensor A and Sensor B), the resonance frequency of the sensors declines as the applied pressure increases. However, the overall frequency shift in Sensor B within the pressure ranging from 0-70 mmHg is greater than that of Sensor A. As can be seen from Figs. 22(b) and 23(b), the phase of the input impedance shows a dip near the resonance frequency of the sensor and decreases as the pressure raises. Study of the reflection coefficient shows that the reflection phase of the sensors increases as the applied pressure increases. The change in the reflection phase of the sensors can be explained by a change in the reactive characteristics of the load (LC tank circuit) under the applied pressure. The measurement results with both sensors are summarized in Table 3. As presented in the table, the overall change in the impedance phase and reflection phase varies as the frequency of the excitation (operation frequency) increases. Nevertheless, the impact of the higher operation frequency is significant in data derived from the resonance frequency shift [I], [IV], [V]. Therefore, it can be interpreted that increasing the operation frequency can improve the sensitivity of the ICP measurement.

In Figs. 22(a) and 23(a), a sudden jump in the resonance frequency of the sensors can be seen, when they are attached to the wall of the water tank. In fact, when the LC sensor is placed near the water tank, the electric flux around the inductive coil reduces due to the permittivity of water. Moreover, the proximity of the sensor to water adds additional parasitic capacitance to the inductive coil and reduces the resonance frequency.

Table 3. Summary of the measurement with Sensor A and Sensor B [I].

Sensor label	Resonance frequency [MHz]	Overall shift in resonance frequency [kHz]	Overall phase dip change [degree]	Overall reflection phase change [degree]	Max. resolution from resonance frequency [mmHg]	Max. resolution from impedance phase [mmHg]	Max. resolution from reflection phase [mmHg]
A	13	280	6.84	0.8	5	2.5	2.5
B	31.2	720	7.51	0.9	2.5	2.5	2.5

4.2 Modeling intraparenchymal and intraventricular ICP measurement

In clinical practice, for intraparenchymal ICP measurement, a pressure sensitive transducer is inserted in the brain parenchyma to measure the compartmental transmittance of ICP. Similar to the intraparenchymal measurement, in intraventricular ICP measurement, a miniature pressure sensitive element is introduced into the ventricle of the brain [69]. Intraventricular ICP monitoring is believed to be the gold standard for assessment of ICP. A graphical illustration of intraventricular and intraparenchymal ICP measurements is shown in Fig. 24. Here, in this study, the performance of the implant (labeled as Sensor C1 in Table 2) was evaluated through specific measurement setups. Two separate measurement setups, named Setup A and Setup B, were designed for each mode of ICP measurement. With Setup A and B, the performance of the sensor for intraparenchymal and intraventricular ICP measurements, respectively, were simulated.

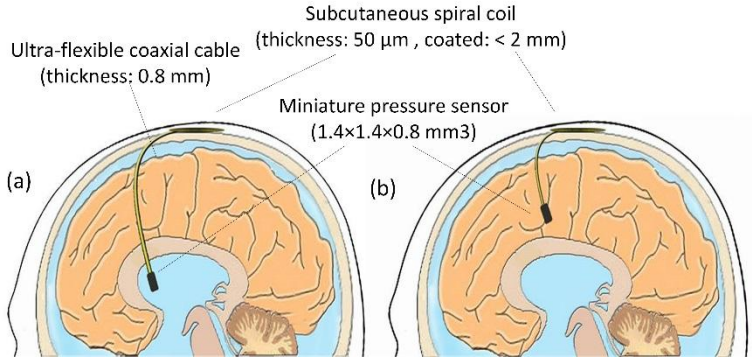

Fig. 24. Graphical illustration of (a) Intraventricular, (b) intraparenchymal ICP measurements [V], ©2016 IEEE.

As depicted in Fig. 25(b), in Setup A, the MEMS pressure sensor was placed inside a balloon filled with a 0.25%-agarose gel. The agarose-filled balloon itself was placed inside a sealed container filled with 0.9 % saline. The agarose gel was used to emulate the viscoelasticity of the brain tissue. In Setup B, the MEMS pressure sensor and the coaxial cable were inserted in the saline container, but without the agarose-filled balloon. In Setup A, the sensing element is in contact with agarose gel, whereas in Setup B, the sensing element is in direct contact with saline. In both setups, the inductive coil of the implant was placed outside the saline container, as shown in Fig. 25(a); the resonance frequency of the sensor was measured using the orthogonal-coil RF probe reported in [59]. The RF probe consists of two orthogonally oriented rectangular coils with separate transmit and receive loops. When an LC-based implant is placed near the RF probe, the resonance frequency of the sensor can be detected by measuring the forward transmission gain (S_{21}) of the probe. The frequency response of the RF probe shows a peak at the resonance frequency of the sensor. The gap between the inductive coil and the RF probe was filled with a saline tub with the height of 5 mm to simulate dissipative properties of the skin. The pressure

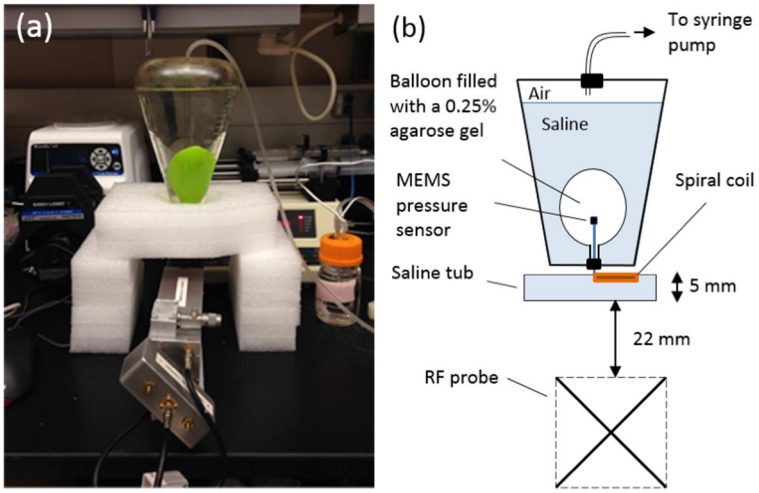

Fig. 25. Modelling intraparenchymal and intraventricular ICP monitoring [III], © 2016 IEEE.

inside the saline container was varied by pressurizing the airtight container within 10-70 mmHg at 5-mmHg intervals and the resonance frequency of the sensor was recorded by measuring the S_{21} parameter of the RF probe using a 50-ohm vector analyzer, provided that transmit and receive loops were connected to port A and port B of the network analyzer, respectively [III].

As shown in Fig. 26, the resonance frequency of the sensor decreases as the applied pressure increases. However, the overall frequency shift within the pressure ranging from 10 to 70 mmHg in Setup A is less than the overall frequency shift in Setup B. The findings from this experiment show that the sensitivity of the pressure-sensing element reduces in agarose gel, indicating that only a part of the applied pressure can deform the diaphragm of the MEMS element. This can be explained by the deformability of the agarose gel. In other words, when the balloon is pressurized through the surrounding liquid, it slightly deforms, which may lead to incomplete transmission of the total pressure to the deformable diaphragm of the MEMS sensor. In addition to the resonance frequency of the sensor, the phase shift of the transmission gain (S_{21}) of the RF probe changes as the pressure varies. This phase shift (phase distortion) can be considered as a variable parameter to the pressure variation through the following definition [III]:

$$PD(\omega) = \varphi|S_{21}(\omega)|^2 \Big|_{\substack{\text{With}\\ \text{sensor}}} - \varphi|S_{21}(\omega)|^2 \Big|_{\substack{\text{Without}\\ \text{sensor}}} \quad (25)$$

A similar trend can be seen from the data obtained from the phase shift. The phase of the S_{21} parameter declines as the pressure increases. As can be seen from Fig. 26, the overall phase distortion (PD) in measurement Setup A and Setup B are 10.42° and 11.33°, respectively [III]. The findings from the *in vitro* test show that the proposed ICP implant is capable of detecting the pressure variation of at least at 5 mmHg intervals in the modeled intraparenchymal and intraventricular ICP measurements, but with different sensitivity.

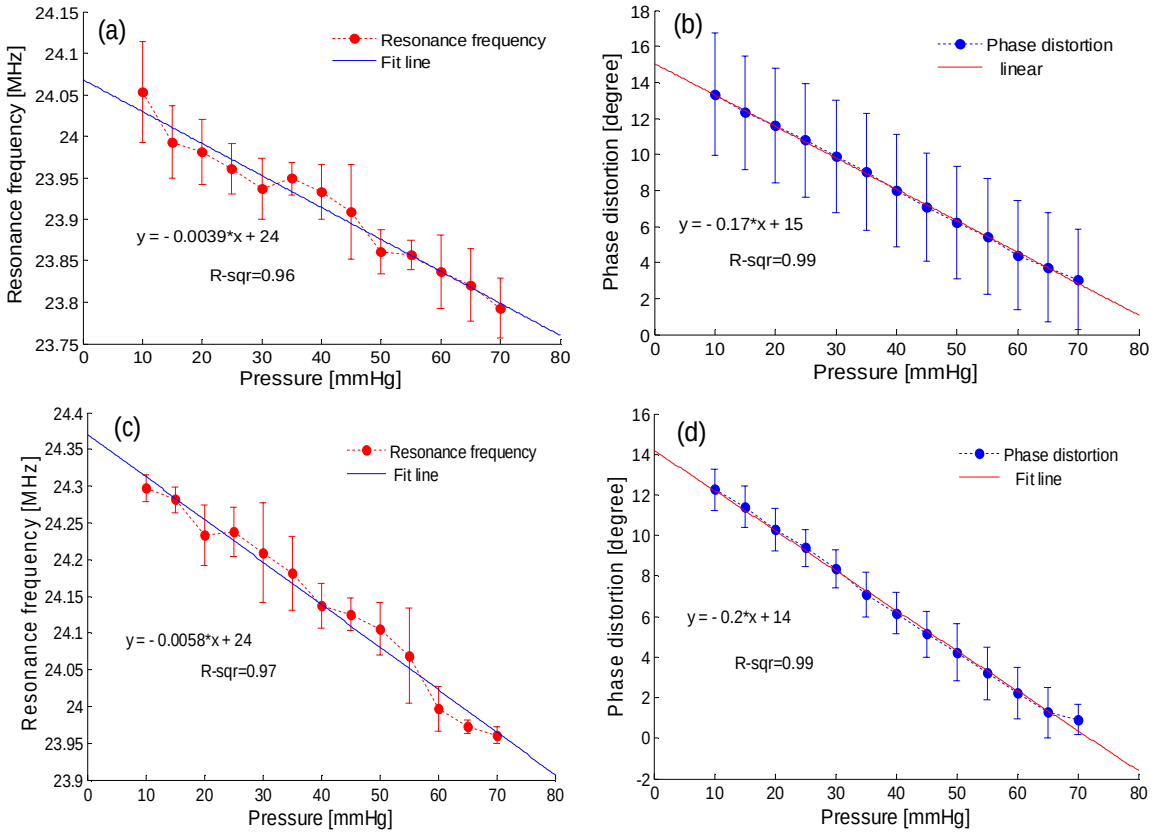

Fig. 26. (a) Resonance frequency versus applied pressure (in Setup A). (b) Phase distortion versus applied pressure (in Setup A). (c) Resonance frequency versus applied pressure (in Setup B). (d) Phase distortion versus applied pressure (in Setup B) [III], © 2016 IEEE.

4.3 Drift performance evaluation

In order to further verify the performance of the sensors before the *in vivo* test, the sensors were tested in a specific measurement setup for long-term drift performance evaluation. In this evaluation test, two identical sensors (labeled as Sensor C2 and Sensor C3 in Table 2) were tested over the course of 40 days and 15 days in a saline container, respectively. Both sensors possess identical geometric properties, but were coated with different materials. The following provides a comprehensive analysis of the drift performance of the sensors.

4.3.1 Analysis of the long-term drift performance of Sensor C2

The performance of Sensor C2 over the course of 40 days is shown in Fig. 27. For a detailed analysis of the sensor's behavior, the graph is divided into Zones 1 and 2, which will be analyzed

separately. The y-axis represents the calculated relative pressure (in mmHg) under the following conditions:

- The inductance of the coil and capacitance of the MEMS sensor (at constant pressure) are constant.
- The ambient pressure (room pressure) was also assumed to be constant and subtracted from the total pressure read by the sensor.

In the measurement with VNA, only the resonance frequency was measured; therefore, the pressure values need to be calculated mathematically through the relation between the applied pressure and capacitance. The relation is given by the MEMS sensor manufacturer as [70]:

$$C_{model}(p) = C_{00} + \frac{C_0}{1 - \frac{C_0}{K}p} + \frac{aC_0}{1 - \frac{C_0}{bK}p} \tag{26}$$

where C_{model} and p are the pressure-dependent capacitance of the MEMS sensor and applied pressure, respectively. C_{00}, C_0 and K are pressure-independent statistical variables and vary from sensor to sensor. Parameters a and b are constants specified by the manufacturer. The only varying parameter is the parasitic capacitance caused by water absorption of the coating material (PDMS for Sensor C2). The parasitic capacitance increases as the coating material absorbs more water.

4.3.1.1 Analysis of Zone 1 and Zone 2 (Sensor C2)

This zone of the graph started with the first day of measurement, when the dry sensor was placed in the water tank at the depth of 20 cm. This height of water creates 15 mmHg hydrostatic pressure. Thus, the applied pressure to the MEMS sensor was 15 mmHg hydrostatic pressure plus

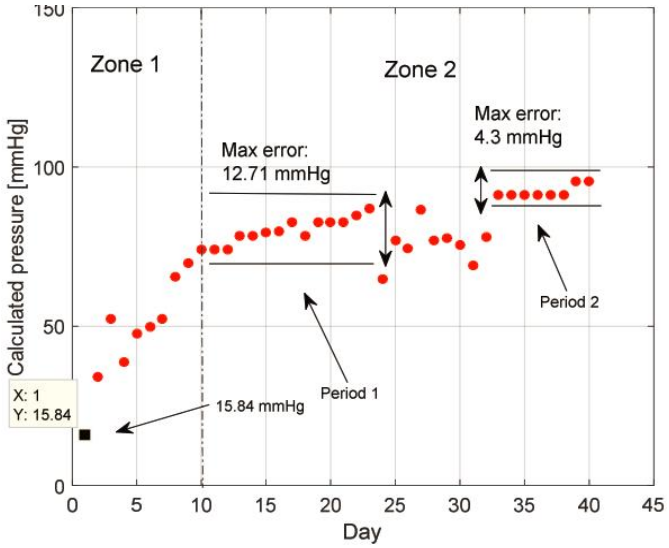

Fig. 27. The drift performance of Sensor C2 over the course of 45 days.

the room pressure. The room pressure (101.045 kPa = 757.9 mmHg) was subtracted from the total pressure read from the sensor.

As can be seen from Fig. 27, the calculated pressure at day 1 is close to 15 mmHg. This is in agreement with the expectations. However, although the pressure was kept constant over the whole period of the study, a major drift from day 1 to day 10 can be seen. This drift occurred due to relatively quick water absorption of the dry sensor. Comparing the slope of the drift in Zone 1 and Zone 2, it can be interpreted that the rate of water absorption reduced after day 10, and consequently, the sensor resonated at a relatively stable frequency.

Zone 2 started from day 10, when the resonance frequency became relatively stable. The maximum drift in period 1 of Zone 2 (14 days) is 12.71 mmHg. The trend of the drift in this period increased, but with a very gentle slope. In period 2 of Zone 2 (8 days), the resonance frequency of the sensor was almost stable, and the maximum drift in the pressure readout was 4.3 mmHg. As can be seen, the pressure value was constant between days 32 to 38, but jumped on days 39 and 40. In the interval between periods 1 and 2, the resonance frequency fluctuated in an irregular pattern. These irregular pressure variations might have occurred because the saline container was emptied and refilled with the same liquid again at day 24.

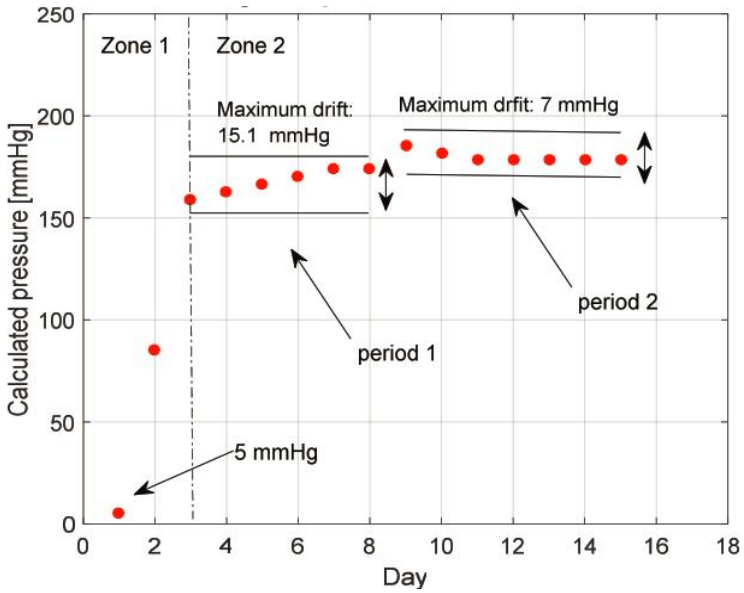

Fig. 28. The drift performance of Sensor C3 over the course of 15 days.

4.3.2 Analysis of the long-term drift performance of Sensor C3

The performance of Sensor C3 is shown in Fig. 28. The measurement procedure for Sensor C3 was the same as Sensor C2, except that Sensor C3 was placed at the depth of 7 cm in the water tank. In addition, Sensor C3 was coated with a biomedical-grade silicon adhesive (Nusil, MED-2000, ε_r=2.66, tan δ=0.007). The total applied pressure to Sensor C3 was the room pressure plus

5 mmHg hydrostatic pressure. The following describes the performance of Sensor C3 in Zones 1 and 2.

4.3.2.1 Analysis of Zone 1 and Zone 2 (Sensor C3)

A similar behavior can be seen with Sensor C3 in Zone 1 (major drift between days 1 to 3). As previously mentioned for Sensor C2, this drift is due to water absorption of the coating material. However, compared to Sensor C2, the resonance frequency of Sensor C3 became stable quicker than Sensor C2. This can be explained by a different rate of water absorption of the different coating materials.

The slope of the drift dramatically reduced in period 1of Zone 2, indicating that the rate of water absorption has decreased. The maximum readout error in this period was 15 mmHg. In period 2 of Zone 2, the resonance frequency of the sensor became almost stable, and the maximum drift in this period is 7 mmHg. As can be seen, the pressure value was completely stable from day 11 onwards.

4.3.3 Conclusion on the drift performance evaluation

The varying parasitic capacitance is the main cause of the measurement drift. The parasitic capacitance changes due to the hydration of the coating material. A major drift can be seen in the first days, and then, the resonance frequency of the sensors eventually become stable. The experimental results showed that the drift in Sensor C3 became stable quicker than Sensor C2. This can be explained by a different rate of water absorption by the different coating materials. According to the findings of this study, the coating material used in Sensor C3 provided more stable encapsulation compared to Sensor C2. Although the resonance frequencies in both sensors became stable after a while, it is not practical to use the sensors for continuous measurement. A possible solution to this issue is to use an auxiliary resonator as the reference point. In the following, the dual-coil operation for drift compensation is described.

4.4 Dual-coil operation for drift compensation

As studied in the previous section, the main challenge in measurement with LC-based sensors is the long-term drift in the resonance frequency. The drift is mainly caused by hydration of the coating material. When the sensor is implanted, the surrounding liquid penetrates the coating material, affecting the dielectric properties of the silicon, which leads to additional parasitic capacitance to the LC circuit, resulting in a reduction of the resonance frequency of the sensor. An illustration of the parasitic capacitance created by coating material is shown in Fig. 29. A practical approach to tackle this issue is to measure the resonance frequency of the sensor against a known reference point. In the proposed method, an auxiliary LC tank circuit with fixed value components forms an independent resonance above the resonance frequency of the sensor to

detect only the drift-related frequency shift caused by the changes in dielectric properties of the coating layer.

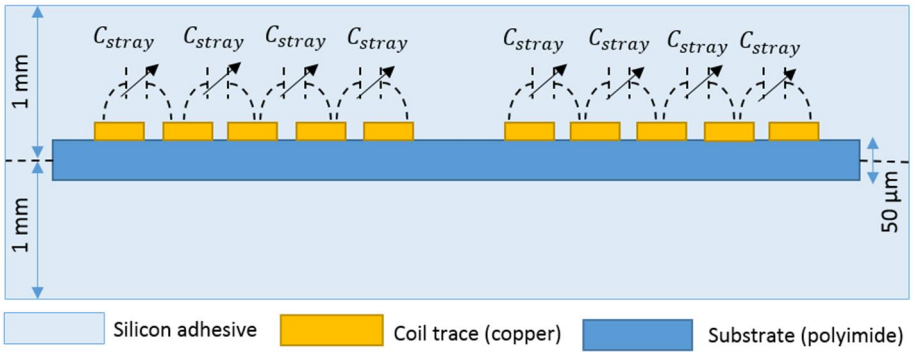

Fig. 29. The stray capacitance between the coil's turn created by coating material.

The principle of the dual-coil operation is illustrated in Fig. 30. This approach relies on the equal impact of liquid absorption on both coils. In other words, the resonance frequency of both LC circuits will be affected equally. As shown in Fig. 30, both peaks shift toward the lower frequencies. However, the rate of the frequency shift differs in the resonators. The best result can be obtained when the following conditions are met: 1) The inductive coil of the reference resonator is identical to the inductive coil of the sensor, to ensure that the impact of the water absorption on both inductors is relatively equal, and 2) The resonance frequency of the reference should be far enough, so that it does not affect the resonance frequency of the sensor and vice versa.

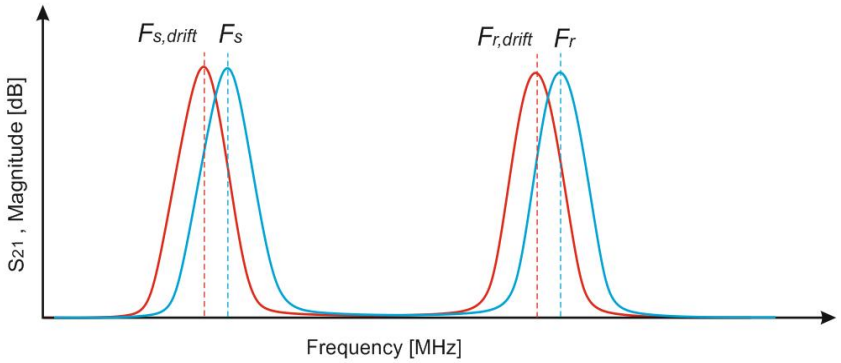

Fig. 30. Impact of the drift-related frequency shift on the resonance frequencies of both resonators.

Considering that the sensor and reference LC circuits form independent resonances, the drift-related frequency shift in each resonator can be defined as

$$\Delta f_s = f_s - f_{s,drift} \tag{27}$$

$$\Delta f_r = f_r - f_{r,drift} \tag{28}$$

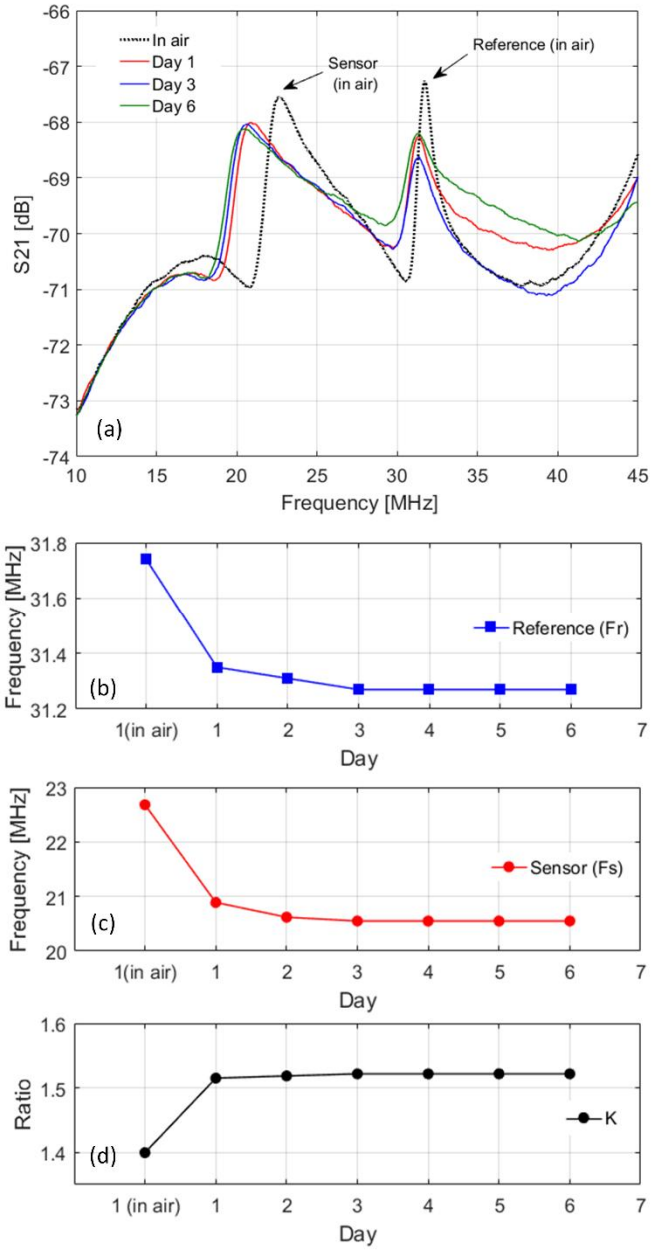

Fig. 31. (a) Frequency response of the implant with two resonators. (b) Resonance frequency of the reference (f_r) versus day. (c) Resonance frequency of the sensor (f_s) versus day. (d) Ratio of the resonance frequencies (K).

where f_s and f_r are the resonance frequencies of the sensor and reference resonator before drift, respectively, and $f_{s,drift}$ and $f_{r,drift}$ represent the resonance frequencies after drift occurs. Recalling Eq. (24) from Chapter 2, the rate of frequency shift with respect to the variation of the capacitance is directly proportional to the resonance frequency. Thus, in order to track only the

drift-related frequency shift of the both resonators, the ratio of the resonance frequencies is defined as

$$K = \frac{f_r}{f_s} = \frac{\Delta f_r}{\Delta f_s}. \tag{29}$$

Since both resonators are affected equally, *K* remains constant, regardless of the amount of drift-related frequency shift if the pressure variation in zero. The determination of pressure-dependent frequency shift in the sensor can be realized through the following relation:

$$\Delta f_{pressure} = \left(f_s - \frac{Df_r}{K}\right) - f_{measured} \tag{30}$$

where $f_{measured}$ is the measured resonance frequency including drift-related and pressure-dependent frequency shifts.

4.5 Performance evaluation of the dual-coil operation

The performance of the dual-coil operation was validated through a test bench. An implant contains a sensor and a reference resonator was fabricated with independent resonance frequencies of around 22.7 and 31.7 MHz, respectively. The resonance frequencies of both resonators were measured in air. Then, the whole device was placed in a saline container, and the resonance frequencies of the devices were measured daily. As can be seen in Fig. 31, both sensor and reference resonators are affected by the surrounding saline, and thereby, both resonance frequencies reduced because of the increasing parasitic capacitance. As can be seen in Figs. 31 (a-c), a major drift occurred between days 1-3, and then the resonance frequencies became stable from day 3 onward. Considering that the pressure was kept constant during the experiment, the frequency shifts have been caused by the variable parasitic capacitance. The drift related frequency-shift was detected through the mathematical calculation described above. As shown in Fig. 31(d), the flat region of the graph indicates that pressure-dependent frequency shift was zero ($\Delta f_{pressure}$). It can be also seen that the ratio of the frequencies (in air) on day 1 does not agree with those of the following days. This can be explained by considering the impact of the hydrostatic pressure on the capacitance of the MEMS sensing element, when the sensor was placed in the saline tank. In other words, for that specific data point, both the hydrostatic pressure and parasitic capacitance contributed to the frequency shift.

5 *In vivo* evaluation

5.1 Device Implantation

The *in vivo* test conducted in this study was the first in-body evaluation of the proposed wireless system to verify the feasibility of a pressure readout. The device implantation was managed by placing a coated, sterilized sensor (labeled as Sensor M1 in Table 2) on the right side of a canine's cranium. The sensor was coated with Biomedical-grade silicon adhesive and sterilized through the Ethylene Oxide (EtO) process. As shown in Fig. 32, the inductive spiral coils were placed between the skin and muscles, and the MEMS sensing element was placed in the subdural region (under the dura) through a small incision. The access to the dura was provided by removing a small bone flap (bone thickness: 3-4 mm) from the skull. With this placement, the MEMS sensing element is in direct contact with CSF to sense ICP and the inductive coils are only a few millimeters (2-3 mm) down under the head skin. The surgical procedure took approximately 1.5 hours to implant the device under general anesthesia. All parts of this animal study were conducted in accordance with the laws and regulations established by Institutional Animal Care

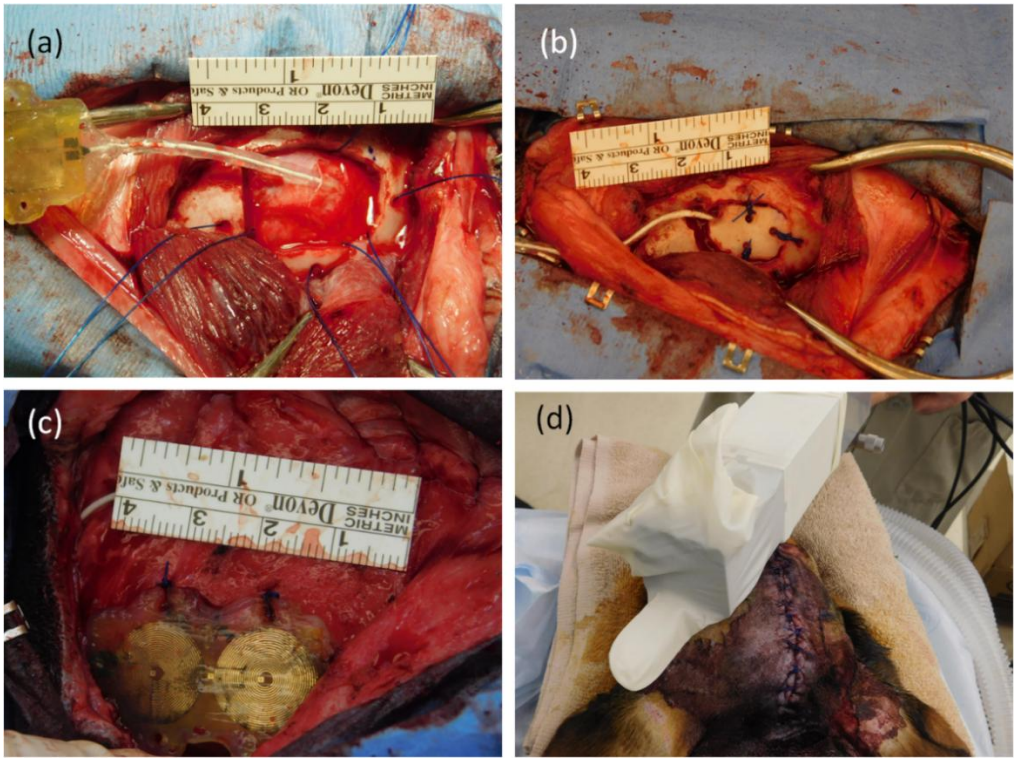

Fig. 32. (a) The MEMS sensing element was placed under the dura through a small incision. (b) After placing the MEMS sensor in the subdural region, the bone flap was sutured to the skull. (c) The coated spiral coils were sutured to the surrounding tissue. (d) The whole device was implanted, and the skin was sutured.

and Use Committee (IACUC) to ensure that the highest ethical standards are met. The specifications of the sensors used in this animal study are presented in Table 4.

Table 4. Specifications of the sensors used in the animal study.

Sensor label in the test	Resonance frequency in air [MHz]	Resonance frequency *in vivo* in head-level position [MHz]	Coil geometry	Length of the coaxial cable [cm]
Sensor M1	21.75	21	Circular	9
Sensor T1	23.48	23.3	Rectangular	6
Sensor T2	23.18	22.9	Rectangular	6

5.2 Wireless measurement with the implant

The wireless pressure readout was conducted by measuring the peak response (i.e. the resonance frequency) of the sensor from approximately 1 cm above the animal's head. A temporary change of ICP was enforced by changing the head's position. To this end, the test bed was tilted upward/ downward (±45°) to alter the ICP level. Elevating the animal's head above cardiac level reduces the ICP by facilitating venous drainage [71]. In contrast, in the head-down position, the ICP level increases. The ICP fluctuation was detected by measuring the resonance frequency of the sensor in head-up and head-down positions and comparing the results with the resonance frequency of the sensor in head-level position. As shown in Fig. 33(b), in the head-up position, the resonance frequency of the sensor increases by +150 kHz, and, in head-down position, it decreases by -150 kHz with respect to the resonance frequency of the sensor in head-level position. According to the measurement results, the *in vivo* performance of the sensor agrees with the *in vitro* data

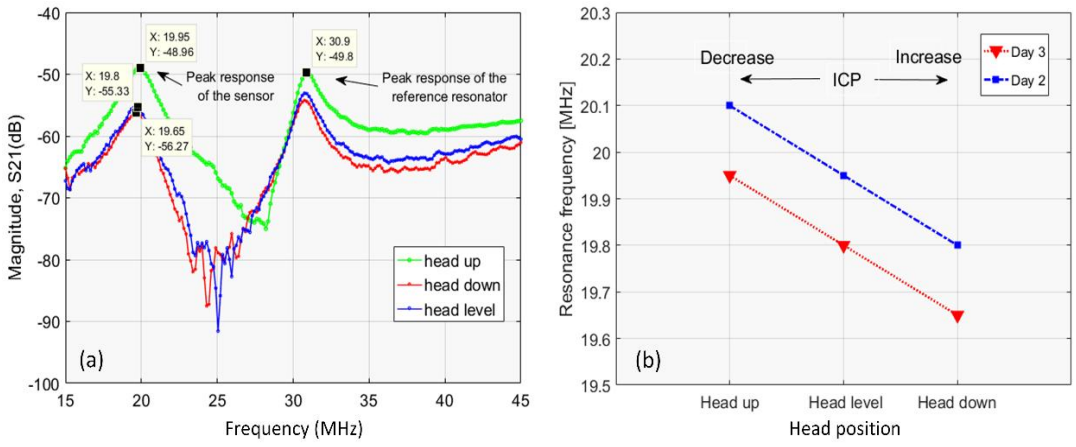

Fig. 33. (a) Frequency response of Sensor M1 in different head positions. (b) Frequency shift versus head position.

obtained from the same sensor. Here, it is relevant to remember that the resonance frequency of the sensor reduces when the applied pressure increases and vice versa.

5.3 Termination of the *in vivo* study and sensitivity test

The *in vivo* study was terminated 2 weeks after the implantation. The ICP implant remained functional until day 4, provided that the day of surgery is counted as day 1. At day 5, wireless reading was not possible with the sensor, and the implant did not respond to external interrogator. At this point, there was an assumption that the implant's function might have been affected by some unknown physiological conditions imposed by post-surgery complications. Therefore, the test was terminated 10 days after the last day of the sensor's active life to ensure that the sensor's status would not change. In the termination of the test, two new implants (labeled as Sensor T1 and Sensor T2 in Table 2) were implanted in the canine's cranium to perform a sensitivity test. Similar to the first implanted device, the capacitive sensing elements of the new implants were placed under the dura. Moreover, a commercial ICP probe was placed into the subdural region next to the sensing elements of the implants. For the sensitivity test, the primary approach to alter the ICP level was to perform hypo/hyper ventilation. However, this method did not change the ICP level in the canine. To tackle this issue, the ICP level was forced to change by tilting the test bed and changing the head position. As mentioned previously, for the sensitivity test, a commercial ICP device (Codman ICP monitor [72]) was used along with the proposed implants to verify their performance.

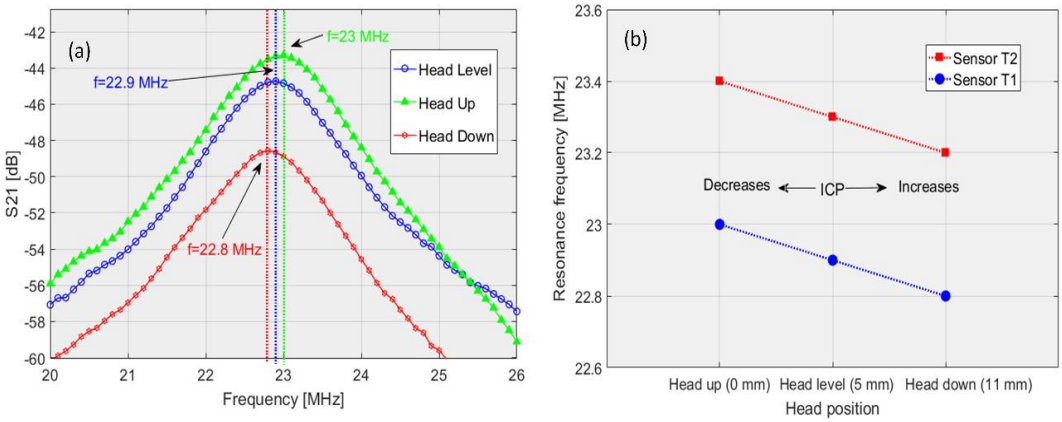

Fig. 34. (a) Peak response of Sensor T2 in different head positions. (b) Frequency shift in Sensor T1 and Sensor T2 versus the head position.

As can be seen from Fig. 34, both devices (Sensor T1 and Sensor T2) showed similar performance to the first implanted device (Sensor M1). The resonance frequency of both sensors declines in the head-down position and increases in the head-up position. A sensitivity of 100 kHz frequency shift was observed per almost 5-mmHg ICP change in both increasing and decreasing gradients. The actual ICP values in different head positions were recorded by the commercial ICP device

(presented in the x-axis of the graph in Fig. 34(b)). The measured ICP values with the commercial device also confirm that ICP level increases in the head-down position and decreases in the head-up position.

5.4 Dielectric properties of the coating material and drift measurement

As previously observed in the drift evaluation test, the coating material (silicon adhesive) may absorb bodily fluids, and consequently, the dielectric properties of the coating material might be affected. This may cause a drift in the resonance frequency and measurement error with the ICP implant. To mitigate the impact of the drift, as described in Chapter 4, a fixed-frequency auxiliary LC tank was used along with the sensor as the reference resonator. The drift cancellation method relies on the equal impact of the drift on the both resonators. This approach was implemented and tested in the *in vivo* evaluation of the implant. As shown in Fig. 35, the ratio of the drift-related frequency shift in the sensor and reference resonators is almost constant over time, suggesting that with the proposed method, the drift-related frequency shift can be detected to correct the measured value through the mathematical calculation explained in the previous chapter.

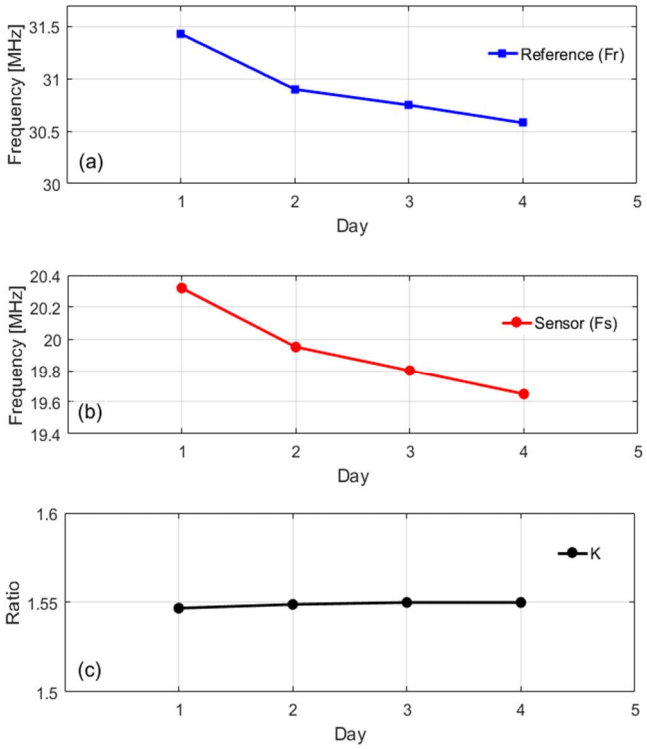

Fig. 35. (a) Drift-related frequency shift of the reference. (b) Drift in the resonance frequency of the sensor. (c) The ratio of the resonance frequencies (*K*). (Data obtained from Sensor M1).

5.5 Conclusion on the *in vivo* evaluation of the ICP implant

The performance of the proposed ICP system was evaluated *in vivo* in a canine model. The finding of the animal study confirmed the concept and feasibility of the wireless ICP readout through the proposed RF telemetry system. The first implanted device remained functional for 4 days. The measurement data obtained from the implant during its active lifetime is consistent with the *in vitro* studies and theoretical analysis of the proposed telemetry system. A probable reason for the implant to turn into inactive mode could be bodily fluids/ CSF penetration into the MEMS sensor or the inductive coil. Therefore, further investigation into the coating procedure and encapsulation of the implant is required in future studies to ensure that the implant can stay functional for the targeted lifetime.

At the end of the animal study, two additional sensors were used to perform the sensitivity test. The data recorded in the sensitivity test were compared with the data recorded by the commercial ICP monitor. A comparison between the data obtained from the sensors in the sensitivity test and data recorded by the ICP monitor confirms the proper performance of the ICP implants. The observations from the animal study are promising, suggesting that after further development, the proposed ICP system can potentially be utilized in real-life biomedical applications.

6 Conclusion

Wireless measurement of physiological parameters in challenging locations of the human body may require implantable devices to perform the measurement. In this doctoral research, a complete wireless solution for ICP monitoring was proposed. The proposed system consists of a battery-less implant, a hand-held reader device and dedicated PC software for real-time ICP monitoring.

The inductive LC-based sensors benefit from simplicity in design and analysis of sensor behavior. This type of sensor is also cost-efficient and easy to fabricate. However, there are challenges associated with this method. The read range of this type of sensor is highly dependent on the strength of the inductive link between the implant and the external reader. Moreover, when implanted, the long-term drift of the sensor is a major source of measurement error. In this research, a novel approach to tackle this issue was proposed and implemented. To mitigate the impact of the drift-related error, an auxiliary resonator with a fixed resonance frequency was used as a reference point for ICP readout. This approach works based on the equal impact of the drift on both resonators and makes it possible to distinguish between the drift-related and pressure-dependent frequency shift.

The proposed reader is a stand-alone device for communication with the ICP implant. The reader device utilizes two separate channels for simultaneous excitation of the sensor and receiving the signal from the implant. The concurrent transmission and receive operation is performed through the dual-port planar antenna. The proposed planar antenna benefits from an innovative topology, which provides T/R isolation with a planar geometry. The planar geometry of the antenna allows for wearable implementation of the antenna. The same platform with minor customization can be used for any other LC-based sensors whose operation principle is based on the inductive coupling.

The *in vivo* performance of the sensor was tested on a canine model and the measurement data obtained from the passive ICP sensor was compared with the data recorded from a commercial ICP monitor. The findings from the *in vivo* study proved the concepts of biotelemetry ICP measurement through inductive link, suggesting that the proposed system can potentially be used for early detection of elevated ICP in patients with TBI, hydrocephalus and chronic intracranial hypertension. In addition, the proposed device can be used alongside a ventricular shunt for continuous monitoring of its performance.

6.1 Future direction

Although the LC-based sensors provide fully passive operation and continuous *in vivo* measurement of physiological parameters, the feasibility of wireless operation is highly dependent on the depth of implantation. In order to be able to detect the miniature sensors in deeper locations of the human body, the range of the wireless operation should be extended. To achieve this goal, the quality factor of the sensor and the geometric properties of the reader antenna need to be optimized for each specific application. Moreover, as mentioned previously, the sensitivity of the pressure measurement depends on the operation frequency of the LC sensor, meaning that higher sensitivity can be achieved by increasing the resonance frequency of the sensor. However, the commercial MEMS sensor used in this study shows significant lossy behavior at higher frequencies. This degrades the quality factor of the resonator and imposes low operation frequency. Therefore, in order to increase the read range and sensitivity, an improved capacitive MEMS pressure sensor (with minimized loss) needs to be designed and customized for this specific application. Moreover, further investigation may be directed at the coating material and sealing procedure to ensure that the implant remains functional for the targeted lifetime.

References

References related to author's papers supporting the thesis manuscript:

I. **M. H. Behfar**, T. Björninen, E. Moradi, L. Sydänheimo and L. Ukkonen, "Biotelemetric Wireless Intracranial Pressure Monitoring: An In Vitro Study," International Journal of Antennas and Propagation, vol. 2015, Article ID 918698, 10 pages, Nov. 2015.

II. **M. H. Behfar**, L. Sydänheimo, S. Roy, and L. Ukkonen, "Dual-Port Planar Antenna for Implantable Inductively Coupled Sensors," IEEE Transaction on Antennas and Propagation, vol. 65, no. 11, pp. 5732–5739, Nov. 2017.

III. **M. H. Behfar**, E. Abada, L. Sydänheimo, K. Goldman, A. J. Fleischman, N. Gupta, L. Ukkonen, and Shuvo Roy, "Inductive passive sensor for intraparenchymal and intraventricular monitoring of intracranial pressure," in 2016 IEEE 38th Annual International Conference of the Engineering in Medicine and Biology Society (EMBC), pp. 1950–1954, 2016.

IV. M. W. A. Khan, **M. H. Behfar**, T. Björninen, L. Sydänheimo, and L. Ukkonen, "Effect of magnetic core and higher operational frequency on sensitivity in frequency shift detection in wireless passive minimally invasive Intracranial Pressure Monitoring," in 2015 International Conference on Electromagnetics in Advanced Applications (ICEAA), pp. 383–386, 2015.

V. **M. H. Behfar**, E. Moradi, T. Björninen, L. Sydänheimo, and L. Ukkonen, "Design and Technical Evaluation of an Implantable Passive Sensor for Minimally Invasive Wireless Intracranial Pressure Monitoring," in World Congress on Medical Physics and Biomedical Engineering, Toronto, Canada, D. A. Jaffrey, Ed. Springer International Publishing, pp. 1301–1304, 2015.

References other than the author's papers:

[1] D. C. Bock, A. C. Marschilok, K. J. Takeuchi, and E. S. Takeuchi, "Batteries used to Power Implantable Biomedical Devices," *Electrochimica Acta*, vol. 84, Dec. 2012.

[2] R. A. Bullen, T. C. Arnot, J. B. Lakeman, and F. C. Walsh, "Biofuel cells and their development," *Biosens. Bioelectron.*, vol. 21, no. 11, pp. 2015–2045, May 2006.

[3] M. Nathan, "Microbattery technologies for miniaturized implantable medical devices," *Curr. Pharm. Biotechnol.*, vol. 11, no. 4, pp. 404–410, Jun. 2010.

[4] K. Dong, B. Jia, C. Yu, W. Dong, F. Du, and H. Liu, "Microbial fuel cell as power supply for implantable medical devices: a novel configuration design for simulating colonic environment," *Biosens. Bioelectron.*, vol. 41, pp. 916–919, Mar. 2013.

[5] X. Wei and J. Liu, "Power sources and electrical recharging strategies for implantable medical devices," *Front. Energy Power Eng. China*, vol. 2, no. 1, pp. 1–13, Mar. 2008.

[6] J. Drews, G. Fehrmann, R. Staub, and R. Wolf, "Primary batteries for implantable pacemakers and defibrillators," *J. Power Sources*, vol. 97, pp. 747–749, Jul. 2001.

[7] C. L. Schmidt and P. M. Skarstad, "The future of lithium and lithium-ion batteries in implantable medical devices," *J. Power Sources*, vol. 97, pp. 742–746, Jul. 2001.

[8] C. F. Holmes, "The role of lithium batteries in modern health care," *J. Power Sources*, vol. 97, pp. 739–741, Jul. 2001.

[9] V. S. Mallela, V. Ilankumaran, and N. S. Rao, "Trends in Cardiac Pacemaker Batteries," *Indian Pacing Electrophysiol. J.*, vol. 4, no. 4, pp. 201–212, Oct. 2004.

[10] A. Kiourti and K. S. Nikita, "A Review of In-Body Biotelemetry Devices: Implantables, Ingestibles, and Injectables," *IEEE Trans. Biomed. Eng.*, vol. 64, no. 7, pp. 1422–1430, Jul. 2017.

[11] S. Ozeri and D. Shmilovitz, "Ultrasonic transcutaneous energy transfer for powering implanted devices," *Ultrasonics*, vol. 50, no. 16, pp. 556–566, Nov. 2009.

[12] T. Maleki, N. Cao, S. H. Song, C. Kao, S. C. Ko, and B. Ziaie, "An Ultrasonically Powered Implantable Micro-Oxygen Generator (IMOG)," *IEEE Trans. Biomed. Eng.*, vol. 58, no. 11, pp. 3104–3111, Nov. 2011.

[13] D. Seo *et al.*, "Wireless Recording in the Peripheral Nervous System with Ultrasonic Neural Dust," *Neuron*, vol. 91, no. 3, pp. 529–539, Aug. 2016.

[14] "Power and Interactive Information Transmission to Implanted Medical Device Using Ultrasonic," *Jpn. J. Appl. Phys.*, vol. 41, no. 5S, p. 3600, May 2002.

[15] A. K. RamRakhyani, S. Mirabbasi, and M. Chiao, "Design and Optimization of Resonance-Based Efficient Wireless Power Delivery Systems for Biomedical Implants," *IEEE Trans. Biomed. Circuits Syst.*, vol. 5, no. 1, pp. 48–63, Feb. 2011.

[16] R. R. Harrison, “Designing Efficient Inductive Power Links for Implantable Devices,” in *2007 IEEE International Symposium on Circuits and Systems*, 2007, pp. 2080–2083.

[17] R. F. Xue, K. W. Cheng, and M. Je, “High-Efficiency Wireless Power Transfer for Biomedical Implants by Optimal Resonant Load Transformation,” *IEEE Trans. Circuits Syst. Regul. Pap.*, vol. 60, no. 4, pp. 867–874, Apr. 2013.

[18] K. van Schuylenbergh and R. Puers, *Inductive Powering: Basic Theory and Application to Biomedical Systems*. Springer Science & Business Media, 2009.

[19] Z. Yang, W. Liu, and E. Basham, “Inductor Modeling in Wireless Links for Implantable Electronics,” *IEEE Trans. Magn.*, vol. 43, no. 10, pp. 3851–3860, Oct. 2007.

[20] U. M. Jow and M. Ghovanloo, “Modeling and Optimization of Printed Spiral Coils in Air, Saline, and Muscle Tissue Environments,” *IEEE Trans. Biomed. Circuits Syst.*, vol. 3, no. 5, pp. 339–347, Oct. 2009.

[21] R. Jegadeesan and Y. X. Guo, “Topology Selection and Efficiency Improvement of Inductive Power Links,” *IEEE Trans. Antennas Propag.*, vol. 60, no. 10, pp. 4846–4854, Oct. 2012.

[22] J. S. Ho, S. Kim, and A. S. Y. Poon, “Midfield Wireless Powering for Implantable Systems,” *Proc. IEEE*, vol. 101, no. 6, pp. 1369–1378, Jun. 2013.

[23] Z. Popović, E. A. Falkenstein, D. Costinett, and R. Zane, “Low-Power Far-Field Wireless Powering for Wireless Sensors,” *Proc. IEEE*, vol. 101, no. 6, pp. 1397–1409, Jun. 2013.

[24] C. Liu, Y. X. Guo, H. Sun, and S. Xiao, “Design and Safety Considerations of an Implantable Rectenna for Far-Field Wireless Power Transfer,” *IEEE Trans. Antennas Propag.*, vol. 62, no. 11, pp. 5798–5806, Nov. 2014.

[25] I. Hochmair *et al.*, “MED-EL Cochlear Implants: State of the Art and a Glimpse Into the Future,” *Trends Amplif.*, vol. 10, no. 4, pp. 201–219, Dec. 2006.

[26] J. F. Patrick, P. A. Busby, and P. J. Gibson, “The development of the Nucleus Freedom Cochlear implant system,” *Trends Amplif.*, vol. 10, no. 4, pp. 175–200, Dec. 2006.

[27] M. Luo, A. W. Martinez, C. Song, F. Herrault, and M. G. Allen, “A Microfabricated Wireless RF Pressure Sensor Made Completely of Biodegradable Materials,” *J. Microelectromechanical Syst.*, vol. 23, no. 1, pp. 4–13, Feb. 2014.

[28] K. Bao *et al.*, “A readout circuit for wireless passive LC sensors and its application for gastrointestinal monitoring,” *Meas. Sci. Technol.*, vol. 25, no. 8, p. 085104, 2014.

[29] K. C. Katuri, M. K. Ramasubramanian, and S. Asrani, “A surface micromachined capacitive pressure sensor for intraocular pressure measurement,” in *Proceedings of 2010 IEEE/ASME International Conference on Mechatronic and Embedded Systems and Applications*, 2010, pp. 149–154.

[30] L. Rosengren, Y. Backlund, T. Sjostrom, B. Hok, and B. Svedbergh, “A system for wireless intra-ocular pressure measurements using a silicon micromachined sensor,” *J. Micromechanics Microengineering*, vol. 2, no. 3, p. 202, 1992.

[31] J. Park, J.-K. Kim, S. J. Patil, J.-K. Park, S. Park, and D.-W. Lee, “A Wireless Pressure Sensor Integrated with a Biodegradable Polymer Stent for Biomedical Applications,” *Sensors*, vol. 16, no. 6, Jun. 2016.

[32] N. Xue, J. B. Lee, S. Foland, and S. P. Chang, “Biocompatible polymeric wireless pressure sensor for intraocular pressure sensing application,” in *2011 IEEE SENSORS Proceedings*, 2011, pp. 1748–1751.

[33] J. Zhai, T. V. How, and B. Hon, “Design and modelling of a passive wireless pressure sensor,” *CIRP Ann. - Manuf. Technol.*, vol. 59, no. 1, pp. 187–190, Jan. 2010.

[34] R. Puers, G. Vandevoorde, D. D. Bruyker, R. Puers, and G. Vandevoorde, “Electrodeposited copper inductors for intraocular pressure telemetry,” *J. Micromechanics Microengineering*, vol. 10, no. 2, p. 124, 2000.

[35] P.-J. Chen, D. C. Rodger, S. Saati, M. S. Humayum, and Y.-C. Tai, “Microfabricated Implantable Parylene-Based Wireless Passive Intraocular Pressure Sensors - Semantic Scholar,” *J. Microelectromechan*, vol. 17, no. 6, pp. 1342–1351, Dec. 2008.

[36] M. A. Fonseca, M. G. Allen, J. Kroh, J. White, "Flexible wireless passive pressure sensors for biomedical applications", Proc. 12th Solid-State Sens. Actuators Microsyst. Workshop, pp. 37-42, 2006-Jun.-48.

[37] L. Y. Chen *et al.*, “Continuous wireless pressure monitoring and mapping with ultra-small passive sensors for health monitoring and critical care,” *Nat. Commun.*, vol. 5, Oct. 2014.

[38] G. Chitnis, T. Maleki, B. Samuels, L. B. Cantor, and B. Ziaie, “A minimally invasive implantable wireless pressure sensor for continuous IOP monitoring,” *IEEE Trans. Biomed. Eng.*, vol. 60, no. 1, pp. 250–256, Jan. 2013.

[39] L. A. Ferrara *et al.*, “A preliminary biomechanical evaluation in a simulated spinal fusion model,” *J. Neurosurg. Spine*, vol. 7, no. 5, pp. 542–548, Nov. 2007.

[40] P. J. Chen, S. Saati, R. Varma, M. S. Humayun, and Y. C. Tai, “Wireless Intraocular Pressure Sensing Using Microfabricated Minimally Invasive Flexible-Coiled LC Sensor Implant,” *J. Microelectromechanical Syst.*, vol. 19, no. 4, pp. 721–734, Aug. 2010.

[41] W. T. Abraham *et al.*, “Wireless pulmonary artery haemodynamic monitoring in chronic heart failure: a randomised controlled trial,” *The Lancet*, vol. 377, no. 9766, pp. 658–666, Feb. 2011.

[42] M. Husák, “One-chip integrated resonance circuit with a capacitive pressure sensor,” *J. Micromechanics Microengineering*, vol. 7, no. 3, p. 173, 1997.

[43] “Hermetically Sealed Inductor-Capacitor (LC) Resonator for Remote Pressure Monitoring,” *Jpn. J. Appl. Phys.*, vol. 37, no. 12S, p. 7124, Dec. 1998.

[44] N. Xue, S. P. Chang, and J. B. Lee, “A SU-8-Based Microfabricated Implantable Inductively Coupled Passive RF Wireless Intraocular Pressure Sensor,” *J. Microelectromechanical Syst.*, vol. 21, no. 6, pp. 1338–1346, Dec. 2012.

[45] Q. A. Huang, L. Dong, and L. F. Wang, “LC Passive Wireless Sensors Toward a Wireless Sensing Platform: Status, Prospects, and Challenges,” *J. Microelectromechanical Syst.*, vol. 25, no. 5, pp. 822–841, Oct. 2016.

[46] St. Jude Medical, “The CardioMEMS^{TM} HF System.” [Online]. Available: https://www.sjm.com/en/sjm/cardiomems. [Accessed: 01-Jul-2017].

[47] L. T. Dunn, “Raised Intracranial Pressure,” *J. Neurol. Neurosurg. Psychiatry*, vol. 73, no. suppl 1, pp. i23–i27, Sep. 2002.

[48] R. M. Chesnut *et al.*, “A Trial of Intracranial-Pressure Monitoring in Traumatic Brain Injury,” *N. Engl. J. Med.*, vol. 367, no. 26, pp. 2471–2481, Dec. 2012.

[49] P. H. Raboel, J. Bartek, M. Andresen, B. M. Bellander, and B. Romner, “Intracranial Pressure Monitoring: Invasive versus Non-Invasive Methods—A Review,” *Crit. Care Res. Pract.*, vol. 2012, p. e950393, Jun. 2012.

[50] C. Wiegand and P. Richards, “Measurement of intracranial pressure in children: a critical review of current methods,” *Dev. Med. Child Neurol.*, vol. 49, no. 12, pp. 935–941, Dec. 2007.

[51] P. Le Roux, “Intracranial Pressure Monitoring and Management,” in *Translational Research in Traumatic Brain Injury*, D. Laskowitz and G. Grant, Eds. Boca Raton (FL): CRC Press/Taylor and Francis Group, 2016.

[52] H. Kristiansson, E. Nissborg, J. Bartek, M. Andresen, P. Reinstrup, and B. Romner, “Measuring elevated intracranial pressure through noninvasive methods: a review of the literature,” *J. Neurosurg. Anesthesiol.*, vol. 25, no. 4, pp. 372–385, Oct. 2013.

[53] “headsense,” *headsense*. [Online]. Available: http://www.head-sense-med.com/. [Accessed: 12-Oct-2015].

[54] U. Kawoos, M.-R. Tofighi, R. Warty, F. A. Kralick, and A. Rosen, “In-Vitro and In-Vivo Trans-Scalp Evaluation of an Intracranial Pressure Implant at 2.4 GHz,” *IEEE Trans. Microw. Theory Tech.*, vol. 56, no. 10, pp. 2356–2365, Oct. 2008.

[55] X. Meng, K. Browne, S. M. Huang, D. K. Cullen, M. R. Tofighi, and A. Rosen, “Dynamic study of wireless intracranial pressure monitoring of rotational head injury in swine model,” *Electron. Lett.*, vol. 48, no. 7, pp. 363–364, Mar. 2012.

[56] Z. Huixin, H. Yingping, G. Binger, L. Ting, and X. Jijun, “A readout system for passive pressure sensors,” *J. Semicond.*, vol. 34, no. 12, Dec. 2013.

[57] E. Moradi, T. Bjorninen, L. Sydanheimo, and L. Ukkonen, “Analysis of biotelemetric interrogation of chronically implantable intracranial capacitive pressure sensor,” in *2014 IEEE RFID Technology and Applications Conference (RFID-TA)*, 2014, pp. 145–149.

[58] H. A. Wheeler, “Frequency meter,” U. S. Patent 2681434A, Jun. 1954.

[59] J. R. Talman, A. J. Fleischman, and S. Roy, “Orthogonal-coil RF probe for implantable passive sensors,” *IEEE Trans. Biomed. Eng.*, vol. 53, no. 3, pp. 538–546, Mar. 2006.

[60] S. N. Makarov, R. Ludwig, and S. J. Bitar, “Second-Order RLC Circuits,” in *Practical Electrical Engineering*, Springer International Publishing, 2016, pp. 481–522.

[61] E. Moradi *et al.*, “Backscattering Neural Tags for Wireless Brain-Machine Interface Systems,” *IEEE Trans. Antennas Propag.*, vol. 63, no. 2, pp. 719–726, Feb. 2015.

[62] K. C. Katuri, S. Asrani, and M. K. Ramasubramanian, “Intraocular Pressure Monitoring Sensors,” *IEEE Sens. J.*, vol. 8, no. 1, pp. 12–19, Jan. 2008.

[63] N. Shah, M. Etemadi, R. Kant, K. Goldman, and S. Roy, “Quality Factor Optimization of Inductive Antennas for Implantable Pressure Sensors,” *IEEE Sens. J.*, vol. 14, no. 8, pp. 2452–2460, Aug. 2014.

[64] T. H. Lee, “The Design of CMOS Radio-Frequency Integrated Circuits,” *Cambridge Core*, Dec-2003. [Online]. Available: /core/books/design-of-cmos-radiofrequency-integrated-circuits/A81450CAE27BBDD03914214FB8AFF19A. [Accessed: 16-Nov-2017].

[65] ANALOG DEVICE, " RF/IF Gain and Phase Detector," AD9951 datasheet, Feb. 2017 [Rev. C].

[66] ANALOG DEVICE, " Direct Digital Synthesize," AD8302 datasheet, 2002 [Rev. A].

[67] Texas Instruments, " Mixed-Signal Microcontrollers," MSP430f5529 datasheet, March 2009 [Revised Nov. 2015].

[68] ifm electronic gmbh, “Pressure transmitter with ceramic measuring cell," PA3528 datasheet, Nov. 2012.

[69] G. Kasotakis *et al.*, “Intraparenchymal vs extracranial ventricular drain intracranial pressure monitors in traumatic brain injury: less is more?,” *J. Am. Coll. Surg.*, vol. 214, no. 6, pp. 950–957, Jun. 2012.

[70] Murata Electronics Oy, "Pressure Elements", SCB10H Series product family specification, .

[71] D. H. Slatter, *Textbook of Small Animal Surgery*. Elsevier Health Sciences, 2003.

[72] Depuy Synthes, Codman neuro, “ICP Monitoring System.”[Online]. Available: https://emea.depuysynthes.com/hcp/codman-neuro/products/qs/icp-monitoring-system. [Accessed: 15-Aug-2017].

Publications

Publication I

M. H. Behfar, T. Björninen, E. Moradi, L. Sydänheimo and L. Ukkonen, "Biotelemetric Wireless Intracranial Pressure Monitoring: An In Vitro Study," International Journal of Antennas and Propagation, vol. 2015, Article ID 918698, 10 pages, Nov. 2015.

Publication II

M. H. Behfar, L. Sydänheimo, S. Roy, and L. Ukkonen, "Dual-Port Planar Antenna for Implantable Inductively Coupled Sensors," IEEE Transaction on Antennas and Propagation, vol. 65, no. 11, pp. 5732–5739, Nov. 2017.

Publication III

M. H. Behfar, E. Abada, L. Sydänheimo, K. Goldman, A. J. Fleischman, N. Gupta, L. Ukkonen, and Shuvo Roy, "Inductive passive sensor for intraparenchymal and intraventricular monitoring of intracranial pressure," in 2016 IEEE 38th Annual International Conference of the Engineering in Medicine and Biology Society (EMBC), pp. 1950–1954, 2016.

Publication IV

M. W. A. Khan, **M. H. Behfar**, T. Björninen, L. Sydänheimo, and L. Ukkonen, "Effect of magnetic core and higher operational frequency on sensitivity in frequency shift detection in wireless passive minimally invasive Intracranial Pressure Monitoring," in 2015 International Conference on Electromagnetics in Advanced Applications (ICEAA), pp. 383–386, 2015.

Publication V

M. H. Behfar, E. Moradi, T. Björninen, L. Sydänheimo, and L. Ukkonen, "Design and Technical Evaluation of an Implantable Passive Sensor for Minimally Invasive Wireless Intracranial Pressure Monitoring," in World Congress on Medical Physics and Biomedical Engineering, Toronto, Canada, D. A. Jaffrey, Ed. Springer International Publishing, pp. 1301–1304, 2015.

Tampereen teknillinen yliopisto
PL 527
33101 Tampere

Tampere University of Technology
P.O.B. 527
FI-33101 Tampere, Finland

ISBN 978-952-15-4074-5
ISSN 1459-2045